

Landau-Zener transitions and Adiabatic impulse approximation in an array of two Rydberg atoms with time-dependent detuning

Ankita Niranjan,¹ Weibin Li,² and Rejish Nath¹

¹*Indian Institute of Science Education and Research Pune, 411008, India*

²*School of Physics and Astronomy, University of Nottingham, Nottingham, NG7 2RD, United Kingdom*

We study the Landau-Zener (LZ) dynamics comprehensively in a setup of two Rydberg atoms with time-dependent detuning, both linear and periodic, using both the exact numerical calculations as well as the method of adiabatic impulse approximation (AIA). The atomic setup realizes different three-level LZ models, for instance, for vanishingly small Rydberg-Rydberg interactions, it converges to a bow-tie model. For sufficiently large interactions, we have a triangular LZ model. The latter is known to exhibit beats and step patterns in the population dynamics. In general, the LZ dynamics show a non-trivial dependence on the initial state, the quench rate of the detuning across avoided crossings, and the interaction strength. Under suitable criteria, the dynamics are well captured by the AIA especially, at large interactions for which the distinct LZ transitions can be isolated from each other by adiabatic regimes. Finally, we extend the analysis to the periodically driven setup, and based on the driving amplitude, the initial states, and the number of avoided crossings driven across, different scenarios are discussed.

I. INTRODUCTION

Landau-Zener transition (LZT) between two energy levels occurs when a two-level system is driven across an avoided level crossing. The paradigmatic example being the LZ model in which the diabatic energy levels cross each other linearly in time [1, 2]. The latter had been generalized to both multi-level systems [3–17] and many-body setups [18–26]. If driven periodically across an avoided level crossing, the separate LZTs interfere, leading to Landau-Zener-Stückelberg (LZS) interferometry [27]. The LZS interference patterns have been analyzed in various physical setups [16, 27–39]. The interference is attributed to multiple exciting phenomena such as the coherent destruction of tunneling [40], dynamical localization in quantum transport [41], and population trapping [42, 43]. On the application side, the interference features can be utilized to control the qubit states [36, 44, 45].

Different techniques have been employed to analyze the complex dynamics in periodically driven quantum systems [27, 46–48]. The most straight forward approach is to solve the corresponding Schrödinger equation. Sometimes, specific approximation methods can provide significant insights into the mechanisms involved in quantum dynamics. One successful approach is adiabatic impulse approximation (AIA). While using AIA, the time evolution is discretized into adiabatic and non-adiabatic regimes. It has been employed to study quantum systems undergoing a quench [49, 50] or periodically driven across an avoided level crossing or a transition point [46]. It is thereby analyzing the LZTs and quantum phase transitions, including the Kibble-Zurek mechanism [49, 51, 52]. At the impulse point, the transition probability obtained from the LZ model in which the system is driven past the avoided level crossing linearly in time is used [1, 2].

Interacting few or many-body periodically driven quantum systems are known to exhibit a variety of new phenomena [46–48, 53–55]. In this regard, Rydberg-excited atoms constitute an ideal platform for such studies [56]. Strong interactions between two Rydberg atoms can suppress further Ryd-

berg excitations within a finite volume and is called the Rydberg blockade [57–60]. Rydberg blockade and the breaking of the blockade (anti-blockades) [61–63] have been at the heart of the Rydberg based quantum simulators and quantum information applications [56]. For two atoms, it has been proposed that through modulation induced resonances, one can engineer the parameter space for both Rydberg-blockade and anti-blockades [64]. Periodic modulation in detuning can suppress Rabi couplings, which can lead to selective (state-dependent) population trapping. Not only that, periodic driving in Rydberg gases provides us insights into fundamental problems, but also finds applications in developing robust quantum gates [65, 66]. To implement periodic driving in a Rydberg chain, one can modulate the light field, which drives the ground to the Rydberg state transition. Another approach is to apply additional radio-frequency or microwave fields, and they provide off-resonant couplings to other Rydberg states. The two methods respectively create sidebands either in the driving field or in the atomic levels [67, 68]. Rydberg atoms in oscillating electric fields [69] have been explored experimentally for manipulating the dipole-dipole interactions via Förster resonances [70–73]. Adiabatic LZTs across a Förster resonance is probed in an experiment using a frozen pair of Rydberg atoms in which the dipole-dipole interaction is vital [74]. But most of the experiments involving LZTs using Rydberg atoms are limited to either a single Rydberg excitation or conditions in which the Rydberg-Rydberg interactions are non-relevant [43, 75–82].

In this paper, we analyze the dynamics in two two-level atoms in which the ground state is coupled to a Rydberg state with a time-dependent detuning. We consider both linear and periodic variation of detuning in time. Before indulging in the two-atom case, we revisit the AIA for a single two-level atom under both linear variation and periodic modulation of detuning. The exact dynamics are in excellent agreement with the results from the semi-analytical AIA under suitable criteria. Also, we point out the striking similarity between the expression for the excitation probability obtained via AIA for the periodically driven case and the intensity distribution of the narrow, equal-amplitude, multi-slit (or a uniform antenna array)

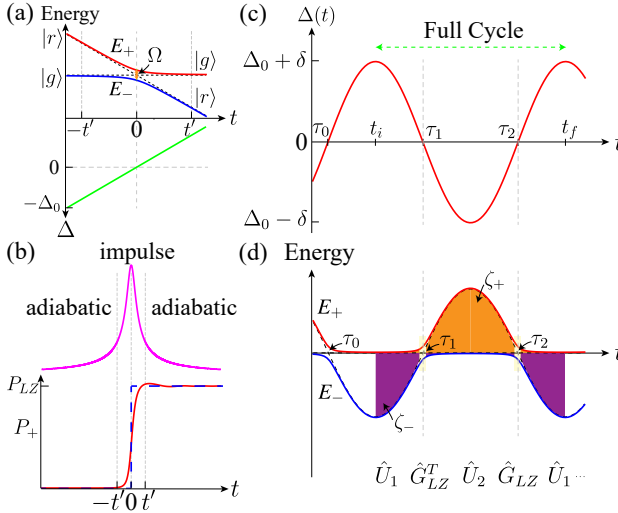


Figure 1. (a) The time-dependent detuning and the instantaneous energy eigenvalues for the linear quench. The dashed lines indicate the diabatic energy levels. (b) shows the inverse of the energy-gap between the adiabatic levels (top one), and based on that, we can approximately distinguish the impulse, and the adiabatic regimes, separated at $\pm t'$. There is no strict definition for t' is used, and while implementing AIA, we take $t' \rightarrow 0$. The bottom plot shows the population in the excited eigenstate ($P_+ = |a_+|^2$) vs time t for an atom initially prepared in the ground state $|\phi_-\rangle$ and is subject to a linear ramp in detuning. Solid line is the numerical solution of the Schrödinger equation and dashed line is the result from the Landau-Zener model [Eq. (3)] showing the asymptotic population ($t \rightarrow \infty$). (c) The periodic time dependence of $\Delta(t)$. (d) The instantaneous energy eigenvalues E_{\pm} for the $\Delta(t)$ in (c). At the avoided level crossings, $t = \tau_{2n}(\tau_{2n+1})$ LZT takes-place and is described by the transition matrix $\hat{G}_{LZ}(\hat{G}_{LZ}^T)$ and either side on it the adiabatic evolution occurs provided by the matrices \hat{U}_1 (lower left side) and \hat{U}_2 (upper right side). The shaded area indicates the accumulated phases (ζ_{\pm}) during the adiabatic evolution.

interference pattern and also the differences. The two-atom setup features three distinct avoided level crossings as a function of the detuning. The avoided level crossings constitute the impulse points at which the LZTs take place. The energy gaps, as well as the separation between the avoided crossings, are highly relevant in determining the population dynamics in both diabatic and adiabatic states. Both the quantities can be modified by varying the interaction strength between the Rydberg excitations. More precisely, it is the ratio between the interaction strength and the square root of the rate at which the system quench across the avoided level crossing is the relevant factor in deciding the nature of the dynamics. In the limit of vanishing interactions, the avoided crossings merge at the point of zero detuning leading to a bow-tie LZ model. In contrast, the strong Rydberg interactions can completely isolate the three avoided crossings from each other, and we realize a triangular LZ model. The latter is known to exhibit beats and step patterns in the population dynamics of adiabatic states.

Using the two-atom model, first, we analyze the population dynamics in a three-level LZ model, and the main features are:

- the LZ dynamics show a non-trivial dependence on

the initial state, the quench rate, and the strength of Rydberg-Rydberg interactions.

- Rabi-like oscillations in diabatic states.
- Sharp LZ transitions between adiabatic states at large Rydberg-Rydberg interactions.
- Analytical predictions are possible using scaling arguments for small Rydberg interactions.
- At sufficiently large interactions, AIA is in excellent agreement with the exact dynamics.
- Interaction independent final population in a doubly ground or doubly excited state.
- Beats in the population dynamics of the singly excited state for the triangular LZ model.

Finally, we extend the analysis to the case in which the detuning is modulated periodically across the avoided level crossings, for large interactions. The latter assures that all three avoided crossings are well isolated, and only involves two adiabatic levels in each of them. When the detuning is modulated across the first avoided crossing, at shorter periods, the dynamics are found identical to that of a two-level atom. At more extended periods, due to resonances, all the three levels become relevant, which also results in the violation of AIA. When the detuning is modulated across either two or all three level crossings, more and more resonances emerge in the population dynamics. The latter also found to be depending on the initial state. For the last case, involving all three avoided crossings, the AIA entirely captures the resulting resonances, whereas in other cases, it does only partially.

The paper is structured as follows. In Section I, we briefly review the dynamics in a two-level atom subjected to time-dependent detuning, both linear and periodic in time. We introduce the concepts of AIA, and the exact numerical results are compared to that of AIA. The validity criteria for AIA is discussed. In Sec. II B results from AIA for a periodically driven atom is compared to the multi-slit interference pattern. In Section III, we extend the studies to the two-atom setup. The three-level LZ model is discussed in Sec. III A. Different cases based on the initial states are considered, and population dynamics in both adiabatic and diabatic basis are discussed. The formation of beats in the population dynamics of the singly excited state is analyzed in Sec. III A 4. In Sec. III A 5, the results from exact numerics for the three-level LZ model is compared to that of AIA. Finally, the periodically driven two Rydberg atoms are considered in Sec. III B, and based on the driving amplitude and the number of avoided crossing are involved, various cases are studied. We summarize in Sec. III C.

II. SINGLE TWO-LEVEL ATOM AND ADIABATIC IMPULSE APPROXIMATION

In this section, we briefly summarize the LZ dynamics in a single two-level atom under both a linear quench and the periodic driving across an avoided level crossing. AIA is then

introduced as a technique to analyze the corresponding dynamics. The two-level atom constitutes of the ground state $|g\rangle$ and a Rydberg state $|r\rangle$, driven by a laser field with a Rabi frequency Ω and a time-dependent detuning $\Delta(t)$. We neglect the motional dynamics of the atom and the system is described by the Hamiltonian ($\hbar = 1$),

$$\hat{H}(t) = \frac{\Omega}{2} \hat{\sigma}_x - \Delta(t) \hat{\sigma}_{rr}, \quad (1)$$

where $\hat{\sigma}_{rr} = |r\rangle\langle r|$ and $\hat{\sigma}_x = |g\rangle\langle r| + |r\rangle\langle g|$ are projection and transition operators, respectively. The states $\{|g\rangle, |r\rangle\}$ form the diabatic basis whereas the adiabatic basis consists of the instantaneous eigenstates of the Hamiltonian, $\hat{H}(t)|\phi_{\pm}(t)\rangle = E_{\pm}(t)|\phi_{\pm}(t)\rangle$. The time-dependent energy eigenvalues are $E_{\pm}(t) = \pm \frac{\Omega}{2} \beta_{\pm}(t)$ with $\beta_{\pm}(t) = [\bar{\Omega}(t) \pm \Delta(t)]/\Omega$ and $\bar{\Omega}(t) = \sqrt{\Delta(t)^2 + \Omega^2}$. $E_{\pm}(t)$ in comparison with the instantaneous detuning is shown in Figs. 1(a) and 1(d) respectively for the linear and the periodic variation of detuning in time. The adiabatic and diabatic bases are related to each other by the time-dependent coefficients $\beta_{\pm}(t)$ via

$$|\phi_{\pm}(t)\rangle = \sqrt{\frac{\Omega}{2\bar{\Omega}}} (\pm \sqrt{\beta_{\pm}} |g\rangle + \sqrt{\beta_{\mp}} |r\rangle), \quad (2)$$

Far away from the avoided level crossings ($|\Delta| \gg \Omega$), the adiabatic levels converge to the diabatic states [see Fig. 1(a)]. The dynamics of the system is governed by the Schrödinger equation: $i\partial/\partial t|\psi(t)\rangle = \hat{H}|\psi(t)\rangle$. Using the adiabatic basis, $|\psi(t)\rangle = a_+(t)|\phi_+(t)\rangle + a_-(t)|\phi_-(t)\rangle$, where $a_{\pm}(t)$ is the time-dependent probability amplitude for finding the atom in the instantaneous adiabatic states $|\phi_{\pm}(t)\rangle$.

A. Adiabatic Impulse Approximation

The basic idea of AIA is to divide the time evolution into adiabatic and non-adiabatic regimes as shown in Fig. 1(b) [27, 83, 84]. In the adiabatic regime, the system remains in the instantaneous eigenstate of the Hamiltonian, whereas in the non-adiabatic or impulse regime, the LZT takes place.

In the LZ model, $\Delta(t) = vt$, where v is the rate at which the detuning is varied across the avoided level-crossing [1, 2]. As seen in Fig. 1(a), the energy gap between the two levels (E_+ and E_-) is maximum in the limit $t \rightarrow \pm\infty$ and is minimum at $t = 0$ with a gap of Ω . The system evolves adiabatically if the rate of change of detuning is lower than the relaxation rate and non-adiabatically otherwise [85]. We approximately show the adiabatic and diabatic regimes in Fig. 1(b) separated at the time t' . The adiabatic region is where $|vt| \gg \Omega$. Assuming the atom is initially in the lowest energy state, the transition probability from the ground to the excited state after a single-sweep across the avoided level crossing is provided by

$$P_{LZ} = \exp\left(-\pi \frac{\Omega^2}{2|v|}\right). \quad (3)$$

For slow quenches ($v \rightarrow 0$), the transition probability to the excited state is minimal ($P_{LZ} \rightarrow 0$). If the quench is very

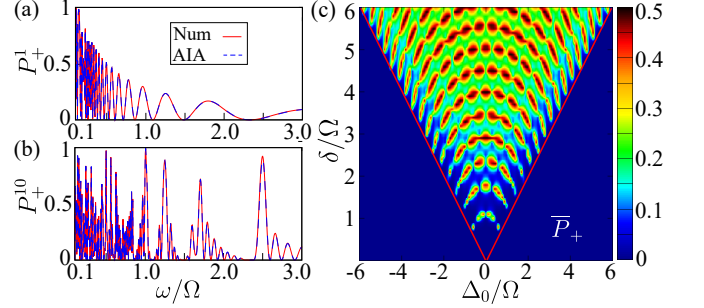


Figure 2. The transition probability to the excited state as a function of ω when the atom is initially prepared in the ground state of \hat{H} for $\delta = 20\Omega$, $\Delta_0 = 5\Omega$, $t_i = \pi/2\omega$ after (a) one cycle and (b) 10 cycles. The solid line is from the numerics, and the dashed line is from the AIA. In (b), the peak at $\omega/\Omega = 2.5$ corresponds to the resonance $2\omega = \Delta_0$ in the fast passage limit. The excellent agreement between the exact dynamics and the AIA is apparent from (a) and (b). (c) Interferometric pattern using AIA: the long-time averaged population in the excited state (\bar{P}_+) as a function of Δ_0/Ω and δ/Ω for $\omega = 0.32\Omega$. The density peaks correspond to the resonance transition between the adiabatic states, and the solid lines mark the validity of AIA.

sudden ($v \rightarrow \infty$), the system makes a complete transition to the excited state ($P_{LZ} \rightarrow 1$). As shown in Fig. 1(d), in the Schrödinger evolution, the dynamics are more involved, especially in the vicinity of the avoided level crossing. Note that the transition mostly takes place across the avoided level crossing, which constitutes the impulse region.

Now, we consider the detuning periodic in time: $\Delta(t) = \Delta_0 + \delta \sin(\omega t)$, where δ and ω are the amplitude and the frequency of the modulation, respectively. When $\Delta(t) = 0$ the system is at the avoided level crossings with an energy gap of Ω , i.e. at times $\tau_{2n} = [2n\pi + \sin^{-1}(-\Delta_0/\delta)]/\omega$ and $\tau_{2n+1} = [(2n+1)\pi - \sin^{-1}(-\Delta_0/\delta)]/\omega$ where $n = 0, 1, 2, \dots$. The atom is taken past the avoided level crossing periodically [see Fig. 1(d)], and in that case, the relative phase of the two levels between the LZTs becomes relevant, especially for the LZS interference [27].

Adiabatic evolution. Between the avoided level crossings, the system undergoes an adiabatic evolution according to $a(t_2) = \hat{U}(t_2, t_1)a(t_1)$ where $a(t) = (a_+(t), a_-(t))^T$ and

$$\hat{U}(t_2, t_1) = \begin{pmatrix} e^{-i\zeta_+} & 0 \\ 0 & e^{-i\zeta_-} \end{pmatrix}$$

with $\zeta_{\pm} = \int_{t_1}^{t_2} dt E_{\pm}(t)$ being the dynamical phases acquired during the time-evolution. In the case of a non-zero bias ($\Delta_0 \neq 0$), the phases acquired, and consequently, the evolution matrices \hat{U}_1 and \hat{U}_2 , for the left and right sides of the crossings are not identical.

Non-adiabatic evolution. In the vicinity of the avoided level crossings, the detuning can be approximated as $\Delta(\tau_n \pm t) \approx \pm vt$ with $v = \omega \sqrt{\delta^2 - \Delta_0^2}$ [27]. It makes the scenario identical to that of the LZ model, and we can use the result given in Eq. (3). Finally, one obtains the non-adiabatic LZT matrix in the

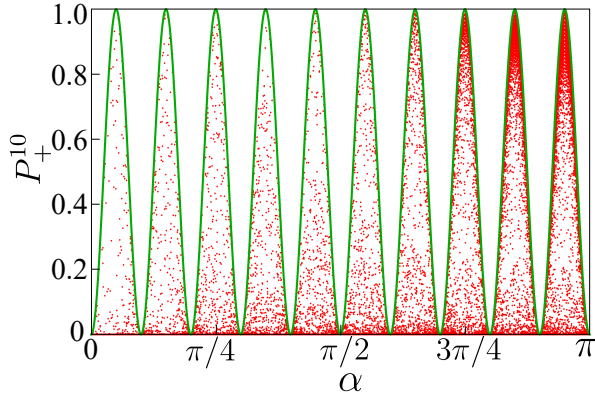


Figure 3. The excitation probability after ten cycles ($k = 10$) as a function of α for $\delta/\Omega = 20$, $\Delta_0 = 0$ and ω is varied. A given α is not associated with a unique value of ω , leading to the scattered red dots, but bounded by the maximum value of $\sin^2 k\alpha$ shown by the solid line.

adiabatic basis $\{| \phi_+ \rangle, | \phi_- \rangle\}$ as,

$$\hat{G}_{LZ} = \begin{pmatrix} e^{-i\tilde{\phi}_s} \sqrt{1 - P_{LZ}} & -\sqrt{P_{LZ}} \\ \sqrt{P_{LZ}} & e^{i\tilde{\phi}_s} \sqrt{1 - P_{LZ}} \end{pmatrix} \quad (4)$$

where the Stokes phase, $\tilde{\phi}_s = \gamma(\ln \gamma - 1) + \arg \Gamma(1 - i\gamma) + \frac{\pi}{4}$ with $\gamma = \Omega^2/4\nu$ being the adiabaticity parameter, and Γ is the gamma function [27]. In terms of γ , the slow and sudden quenches are indicated respectively by $\gamma \gg 1$ and $\gamma \ll 1$.

B. Comparison with Multi-slit interference Pattern

Over a half-cycle, say from $t_i = \tau_1 - \pi/2\omega$ to $t_f = \tau_1 + \pi/2\omega$, we can define the evolution matrix as $\hat{U}_2(t_f, \tau_1)\hat{G}_{LZ}^T\hat{U}_1(\tau_1, t_i)$. In general, the order of the transition and adiabatic matrices should be carefully chosen depending on the initial (t_i) and final (t_f) times, as well as the value of Δ_0 . Similarly, one obtains the evolution matrix for one full cycle, say from $t_i = 0$ to $t_f = 2\pi/\omega$ with $\Delta_0 > 0$ [see Figs. 1(c) and 1(d)] as $\hat{F} = \hat{U}_1(2\pi/\omega, \tau_2)\hat{G}_{LZ}\hat{U}_2(\tau_2, \tau_1)\hat{G}_{LZ}^T\hat{U}_1(\tau_1, 0)$, where the label T stands for the transpose of the matrix. It is required due to the change in sign of ν when $\Delta(t)$ reverses. For the full cycle, the LZTs take place at two instants. Writing the full cycle evolution matrix as:

$$\hat{F} = e^{i\phi_G} \begin{pmatrix} g_{11} & -g_{21}^* \\ g_{21} & g_{11}^* \end{pmatrix} \quad (5)$$

where

$$g_{11} = e^{-i\eta_0}(1 - P_{LZ}) + e^{-i\eta_1}P_{LZ} \quad (6)$$

$$g_{21} = (e^{-i\eta_3} - e^{-i\eta_2})e^{i\tilde{\phi}_s} \sqrt{(1 - P_{LZ})P_{LZ}} \quad (7)$$

where $\phi_G = \exp\left(i \int_0^{2\pi/\omega} \Delta(t)dt/2\right)$, $\eta_0 = \frac{1}{2} \int_0^{2\pi/\omega} \bar{\Omega}dt + 2\tilde{\phi}_s$, $\eta_1 = \frac{1}{2} \int_0^{2\pi/\omega} \bar{\Omega}dt - \int_{\tau_1}^{\tau_2} \bar{\Omega}dt$, $\eta_2 = \frac{1}{2} \int_0^{2\pi/\omega} \bar{\Omega}dt - \int_{\tau_2}^{2\pi/\omega} \bar{\Omega}dt + 2\tilde{\phi}_s$ and $\eta_3 = \int_0^{\tau_1} \bar{\Omega}dt - \frac{1}{2} \int_0^{2\pi/\omega} \bar{\Omega}dt$ are the dynamical phases. Assuming the system is initially prepared in the ground state, the

transition probability to the excited state after one full cycle is given by,

$$P_+^1 = |g_{21}|^2 = 4(1 - P_{LZ})P_{LZ} \sin^2 \phi_s. \quad (8)$$

Eq. (8) implies that the transition probability after one period is the result of the quantum interference between the two transition amplitudes at τ_1 and τ_2 , as well as a periodic function of the phase $\phi_s = \frac{1}{2} \int_{\tau_1}^{\tau_2} \bar{\Omega}dt + \tilde{\phi}_s$, called the Stückelberg phase. Thus, the dynamical phase acquired between the LZTs at τ_1 and τ_2 , and the phase change during the LZTs ($\tilde{\phi}_s$) become highly relevant to characterize the full cycle dynamics. We have constructive (destructive) interference with $|g_{21}|^2 = P_{LZ}$ ($|g_{21}|^2 = 0$) when $\phi_s = (n + 1/2)\pi$ ($\phi_s = n\pi$) where $n = 0, 1, 2, \dots$. As long as the LZT time (the duration for which the LZT happens when the system drives past an avoided crossing) is sufficiently shorter than the duration of adiabatic evolution between the two transitions [$\tau_{LZ} < (\pi - 2 \sin^{-1}(-\Delta_0/\delta))/\omega$], AIA is valid. The upper limit for LZT time, τ_{LZ} is given by $(\sqrt{\gamma}/\Omega) \max(1, \gamma)$. It implies that for sufficiently large values of δ , with small ν (consequently ω) subjected to the criteria $\delta - \Delta_0 > \Omega$ and $\delta\omega > \Omega^2$, AIA is valid [27, 83, 84]. In Fig. 2(a), we show the transition probability to the excited state after a single cycle with $\delta = 20\Omega$, $t_i = \pi/2\omega$, $t_f = 5\pi/2\omega$ and $\Delta_0 = 5\Omega$ when the atom is initially prepared in the ground state. The results from AIA are found to be in an excellent agreement with the exact numerical results obtained by solving the Schrödinger equation.

It is straightforward to extend AIA for multiple cycles, and we have $\hat{F}^k = (\hat{U}_1 \hat{G}_{LZ} \hat{U}_2 \hat{G}_{LZ}^T \hat{U}_1)^k$ for k -cycles. Writing it in the matrix form [27],

$$\hat{F}^k = e^{ik\phi_G} \begin{pmatrix} u_{11} & -u_{21}^* \\ u_{21} & u_{11}^* \end{pmatrix}, \quad (9)$$

where $u_{11} = \cos k\alpha + i\text{Im}(g_{11}) \sin k\alpha / \sin \alpha$ and $u_{21} = g_{21} \sin k\alpha / \sin \alpha$ with $\cos \alpha = \text{Re}(g_{11})$. Therefore the transition probability from the ground to the excited state after k -cycles is

$$P_+^k = |u_{21}|^2 = 4(1 - P_{LZ})P_{LZ} \sin^2 \phi_s \frac{\sin^2 k\alpha}{\sin^2 \alpha} \quad (10)$$

The long-time ($k \gg 1$) averaged occupation probability in the excited state is

$$\bar{P}_+ = \frac{2(1 - P_{LZ})P_{LZ} \sin^2 \phi_s}{\sqrt{[4(1 - P_{LZ})P_{LZ} \sin^2 \phi_s]^2 + \text{Im}(g_{11})^2}}. \quad (11)$$

Thus, a resonant transition between the adiabatic states ($\bar{P}_+ = \bar{P}_- = 1/2$) occurs when $\text{Im}(g_{11}) = -[(P_{LZ}) \sin \eta_1 + (1 - P_{LZ}) \sin \eta_0] = 0$. In the fast passage limit ($\gamma \gg 1$), $(P_{LZ}) \approx 1$, the resonance condition reduces to $\Delta_0 = n\omega$. The peak at $\omega/\Omega = 2.5$ in Fig. 2(b) can be attributed to the resonance $2\omega = \Delta_0$ at which the population is almost completely transferred from the ground to the excited state. In the slow passage limit a simple relation for the resonances are not possible, but can be identified from the density peaks of \bar{P}_+ [see Fig. 2(c)] for smaller values of δ/Ω [86]. In the fast passage limit with

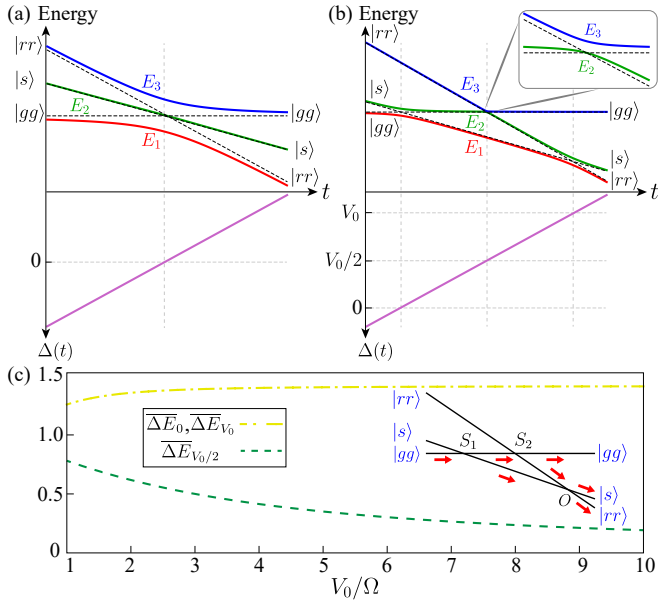


Figure 4. Energy eigenvalues E_j as a function of the instantaneous detuning $\Delta(t) = vt$ for (a) $V_0 = 0.1\Omega$ and (b) $V_0 = 5\Omega$. There exist three avoided level crossings, and they are separated from each other by $V_0/2$. The dashed lines show the diabatic energy levels. Below each plot, we show the linear variation of the detuning $\Delta(t)$. The avoided crossings in (b) form a triangular LZ model. The inset of (b) shows the zoomed-in version of the avoided crossing at $V_0/2$. The asymptotic states at $t \rightarrow \pm\infty$ are shown in the left and right end of the level diagrams. (c) shows the energy gaps $\overline{\Delta E}_a = \Delta E_a/\Omega$ at the avoided crossings as a function of V_0 . The inset shows the schematic setup for the LZ interferometry, in which the first and the second crossings act as the beam splitter. The last crossing at O where the mixing takes place, and any final population in $|gg\rangle$ is the leakage from the interferometry.

$\delta \gg \Omega$, the resonance also implies complete Rabi oscillations between the diabatic states $|g\rangle$ and $|r\rangle$ if initially prepared in one of the states [83].

It is interesting to note the similarity in the form of the Eq. (10) with the intensity distribution of an array of k narrow equal amplitude slits (or an antenna array) interference pattern. For the latter case, the intensity along the direction θ is given by [87],

$$I(\theta) = I_0 \frac{\sin^2(k\phi/2)}{\sin^2(\phi/2)}, \quad (12)$$

where I_0 is the intensity from a single slit. The angle, $\phi = 2\pi d \sin \theta / \lambda$ is the phase difference between the consecutive slits where d is the spacing between the center of the adjacent slits, and λ is the wavelength of light. Neglecting the slit widths (I_0 becomes a constant), the intensity pattern has principal maxima at $\phi = 2n\pi$ where $n = 0, 1, 2, 3, \dots$, and between two principal maxima there are $k - 1$ minima located at $\phi/2 = \pi/N, 2\pi/N, \dots, (N - 1)\pi/N$. Also, there are $N - 2$ secondary maxima between two principal maxima. Though the form of equations is the same, they exhibit significant differences. For instance, I_0 in Eq. (12) does not depend on

ϕ , whereas the corresponding term ($|g_{21}|^2$) in Eq. (10) and α are not independent. In the latter case, a little algebra reveals us that the maxima in the transition probability occur at $\cos k\alpha = 0$ or $\alpha = (2n + 1)\pi/2k$, and the minima occur at $\sin k\alpha = 0$ or $\alpha = n\pi/k$. Thus, $\alpha = 0$ doesn't correspond to a maximum but a minimum, which is in contrast with the antenna array intensity distribution for which $\phi = 0$ represents a principal maximum. The other difference is that there are no secondary maxima in the excitation probability and consequently, one minimum between the maxima. It can be seen in Fig. 3, which shows the results from AIA for the excitation probability after ten cycles ($k = 10$) as a function of α for $\delta/\Omega = 20$, $\Delta_0 = 0$ and ω is varied (similar results can be obtained if δ or Δ_0 is varied). There is no one to one correspondence between α and ω , leading to scattered red dots in Fig. 3. For a fixed α , the maximum value of P_+^k is provided by the condition $\Im(g_{11}) = 0$, and we have $(P_+^k)_{MAX} = \sin^2 k\alpha$, which is shown by the solid line in Fig. 3. As the number of cycles (k) increases, the number of peaks increases and also gets sharper. These results imply that, by correctly choosing the driving parameters, including the number of cycles k , we can control the transition probability in a two-level atom or a qubit. The same results also hold for the periodically driven two-atom case, which will be discussed in Sec. III B 1.

III. TWO TWO-LEVEL ATOMS: RYDBERG-RYDBERG INTERACTIONS

At this point, we extend the above analysis to that for two atoms, and in particular, we include the inter-atomic interactions when the atoms get excited to the Rydberg state. Note that, the two-atom setup with Rydberg excitations has been a usual scenario in many of the recent experimental studies [59, 88–99]. The system is described by the Hamiltonian,

$$\hat{H} = -\Delta(t) \sum_{i=1}^2 \hat{\sigma}_{rr}^i + \frac{\Omega}{2} \sum_{i=1}^2 \hat{\sigma}_x^i + V_0 \hat{\sigma}_{rr}^1 \hat{\sigma}_{rr}^2, \quad (13)$$

where $V_0 = C_6/R^6$ is the Rydberg-Rydberg interaction between the atoms separated by a distance R and C_6 is the van der Waals coefficient which can be either positive or negative depending on the angular momenta of the atomic state [100]. We restrict ourselves to $V_0 > 0$. When $V_0 = 0$, the two atoms are completely decoupled, and each of them exhibits independent but similar LZ dynamics. To analyze the interacting case, we use the diabatic basis $\{|gg\rangle, |s\rangle, |rr\rangle\}$ where $|s\rangle = (|gr\rangle + |rg\rangle)/\sqrt{2}$ is the symmetric state and the asymmetric state $(|gr\rangle - |rg\rangle)/\sqrt{2}$ can be disregarded in our dynamics. The instantaneous eigenstates of the Hamiltonian \hat{H} in the diabatic basis are

$$|j\rangle = \frac{1}{A} \begin{pmatrix} -\frac{V_0 - 2\Delta(t) - E_j}{E_j} \\ -\frac{\sqrt{2}(V_0 - 2\Delta(t) - E_j)}{\Omega} \\ 1 \end{pmatrix} \quad (14)$$

where $j \in \{1, 2, 3\}$, A is the normalization constant and they form the adiabatic basis. Thus, the two-atom setup effectively acts as a three-level system. Asymptotically the

state $|j\rangle$ approaches the diabatic ones as $\lim_{\Delta \rightarrow -\infty} |1\rangle = |gg\rangle$, $\lim_{\Delta \rightarrow \infty} |1\rangle = |rr\rangle$, $\lim_{\Delta \rightarrow \pm\infty} |2\rangle = |s\rangle$, $\lim_{\Delta \rightarrow -\infty} |3\rangle = |rr\rangle$ and $\lim_{\Delta \rightarrow \infty} |3\rangle = |gg\rangle$. Upon diagonalizing the Hamiltonian, the instantaneous eigenenergies E_j are obtained as the roots of the cubic polynomial: $f(x) = -x^3 + (V_0 - 3\Delta)x^2 + (V_0\Delta - 2\Delta^2 + \Omega^2)x - V_0\Omega^2/2 + \Delta\Omega^2$ and we get

$$E_n = \frac{1}{3} [V_0 - 3\Delta + 2|C| \cos(\theta_n/3)] \quad (15)$$

where $\theta_n = 3 \arccos(\Re(C)/|C|) + \lambda_n$ with $\lambda_n = 2(3 - n)\pi$, $C = \left[(D_1 - \sqrt{D_1^2 - 4D_0^3})/2 \right]^{1/3}$, $D_0 = V_0^2 - 3V_0\Delta(t) + 3\Delta(t)^2 + 3\Omega^2$, and $D_1 = 2V_0^3 - 9V_0^2\Delta(t) + 9V_0\Delta(t)^2 - 9V_0\Omega^2/2$.

As a function of Δ , the system exhibits three distinct avoided level crossings and are located at (i) $\Delta = 0$ ($|1\rangle \leftrightarrow |2\rangle$), (ii) $\Delta = V_0/2$ ($|2\rangle \leftrightarrow |3\rangle$) and (iii) $\Delta = V_0$ ($|1\rangle \leftrightarrow |2\rangle$) separated from each other by $V_0/2$. Figs. 4(a)-(b) show the instantaneous energies E_j for the case in which the detuning is varied linearly in time and for two different V_0 . Since the diabatic state $|s\rangle$ couples to both $|gg\rangle$ and $|rr\rangle$, but the latter do not couple to each other; for vanishing interactions our model comes down to so-called the bow-tie model [3, 4, 101, 102]. A four state bow-tie model can be implemented using the same setup if an additional Rabi-offset is provided between the two atoms [17, 103]. In the latter case, our two-atom setup then consists of four energy levels. In terms of spin matrices, the Hamiltonian in Eq. (13) becomes a SU(3) model, by mapping $\{|gg\rangle, |s\rangle, |rr\rangle\} \rightarrow \{|+1\rangle, |0\rangle, |-1\rangle\}$ [8, 9]

$$\hat{H}_s = \left[\Delta(t) - \frac{V_0}{2} \right] \hat{S}_z + \Omega \hat{S}_x + \frac{V_0}{2} \hat{S}_z^2, \quad (16)$$

where \hat{S}_z and \hat{S}_x are the spin-1 matrices, and the last term is generally known as the easy-axis single-ion anisotropy in the context of magnetic systems. In the limit $V_0 \rightarrow 0$, the three avoided level crossings merge and coincide at the point of zero detuning [Fig. 4(a)], and we have a spin-1 SU(2) model [7]. The presence of interaction term V_0 makes the model [Eq. (16)] non-linear in SU(2) basis, but the nonlinearity can be removed by expressing in terms of the generators (Gell-Mann matrices) of the SU(3) group [9]. For sufficiently large V_0 (blockade regime), the avoided level crossings are distinguishable, and they form a triangular geometry [see Fig. 4(b)]. A similar triangle LZ model is analyzed in Ref. [9] and different patterns like beats and steps in the LZ dynamics are predicted depending on the system parameters [9, 16].

A necessary quantity for analyzing LZ dynamics is the energy gaps ΔE_α at the avoided crossings, and ΔE_α as a function of V_0 are shown in Fig. 4(c) where $\alpha \in \{0, V_0/2, V_0\}$ indicates the value of Δ at which the avoided crossing occurs. The gap at the first (ΔE_0) and the last (ΔE_{V_0}) avoided crossings increases with V_0 initially and eventually saturated to $\sqrt{2}\Omega$ at sufficiently large values of V_0 , whereas $\Delta E_{V_0/2}$ decreases inversely with V_0 , i.e., $\Delta E_{V_0/2} \sim 1/V_0$. The vanishingly small $\Delta E_{V_0/2}$ at large V_0 can be associated with the fact that $|gg\rangle$ and $|rr\rangle$ are not directly coupled. In short, V_0 not only isolates the different LZTs from each other but also modifies the energy gaps at the avoided level crossings.

A. Three-level Landau-Zener Model

First, we discuss the three-level LZ model in which the detuning varies linearly in time [3, 6, 7] and from that we extend to the periodically driven case. In the LZ model, the Hamiltonian in the diabatic basis $\{|gg\rangle, |s\rangle, |rr\rangle\}$ is given as

$$\hat{H} = \begin{pmatrix} 0 & \frac{\Omega}{\sqrt{2}} & 0 \\ \frac{\Omega}{\sqrt{2}} & -vt & \frac{\Omega}{\sqrt{2}} \\ 0 & \frac{\Omega}{\sqrt{2}} & -2vt + V_0 \end{pmatrix}.$$

Note that, the energy of $|s\rangle$ state varies at a rate v whereas that of $|rr\rangle$ state is $2v$ compared to $|gg\rangle$. We consider one complete sweep across all the three avoided level crossings from far left to the far right and analyze the LZ dynamics as a function of both v and V_0 for different initial conditions. The non-adiabatic transition amplitudes depend on both V_0 and v . To be more explicit, by using simple scaling arguments (defining $\tilde{t} = t/\sqrt{v}$ in the Schrödinger equation), we argue that the transition probabilities can only be a function of two parameters: Ω/\sqrt{v} and V_0/\sqrt{v} .

$$1. \quad |\psi(t_i)\rangle = |1\rangle$$

Adiabatic basis. The population dynamics in the adiabatic basis, for different v and V_0 in which the system is initially ($t \rightarrow -\infty$) prepared in the ground state $|1\rangle$ are shown in Figs. 5 and 6. The first LZT takes place from $|1\rangle$ to $|2\rangle$ around $t_1 = 0$, the second one from $|2\rangle$ to $|3\rangle$ around $t_2 = V_0/2v$ and the last one is between $|1\rangle$ and $|2\rangle$ around $t_3 = V_0/v$. The state $|3\rangle$ is involved only in one LZT (the second one), whereas $|1\rangle$ and $|2\rangle$ are part of more than one LZTs. The latter implies that the final population in the states $|1\rangle$ and $|2\rangle$, i.e., $P_1(t \rightarrow \infty)$ and $P_2(t \rightarrow \infty)$, is determined by the interference of LZTs at the different avoided crossings. For $V_0 \ll \Omega$ [Fig. 5(a)-(c)], it is not possible to resolve the three different LZTs in time since the avoided level crossings are so closely occurring [Fig. 4(a)]. On the other hand, for any v , we can choose a sufficiently large V_0 such that different LZTs are resolved, as shown in Figs. 5(d)-(i). The first and third transitions can be identified with the two major dips in the population $P_1(t)$ of the state $|1\rangle$, as seen in Figs. 5(d)-(i). The dips correspond to the population transfer from $|1\rangle$ to $|2\rangle$. Once the LZTs are temporally resolved, we have a basic setup for the LZ interferometer based on amplitude splitting. It is schematically shown in the inset of Fig. 4(c). The (avoided) crossings play the role of beam splitters [S_1 and S_2 in Fig. 4(c)], and the energy gaps and the rate of quench can be related to the thickness of the beam splitters. The last crossing at O is where the mixing takes place, and any final population in $|gg\rangle$ is the leakage from the interferometry.

Fig. 5 (along rows) and Fig. 6 reveal that for a given V_0 , faster the linear quench larger the non-adiabatic transition probabilities. The latter results in a larger $P_3(t \rightarrow \infty)$ and a smaller $P_1(t \rightarrow \infty)$, whereas $P_2(t \rightarrow \infty)$ displays a non-monotonous behavior. When the level crossings are well separated and distinguishable in time, which requires V_0/v to

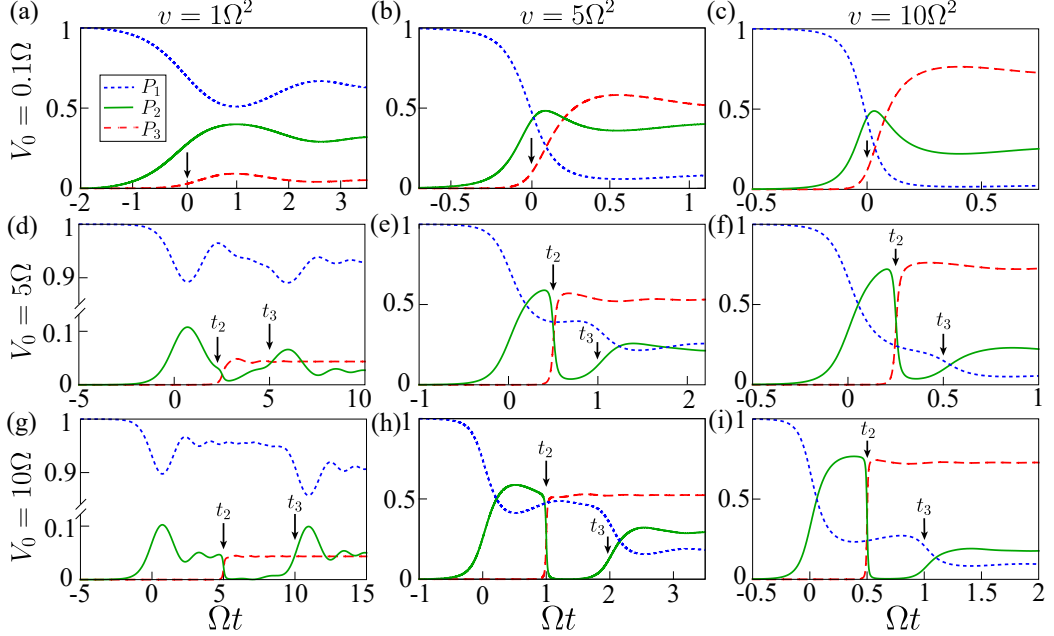


Figure 5. The dynamics of populations P_j in the adiabatic states $|j\rangle$ for the initial state $|\psi(t=0)\rangle = |1\rangle$ with three different values of v and V_0 . The magnitude of v is given in the top, and that of V_0 is given in the left end. The dashed, solid, and dotted-dashed lines show the populations in states $|1\rangle$, $|2\rangle$, and $|3\rangle$ respectively. The first LZT takes place in the vicinity of $t = 0$. The thin arrows show the times around which the second (t_2) and the third (t_3) LZTs occur. In (a)-(c), the LZTs are not resolvable, so a single arrow is shown.

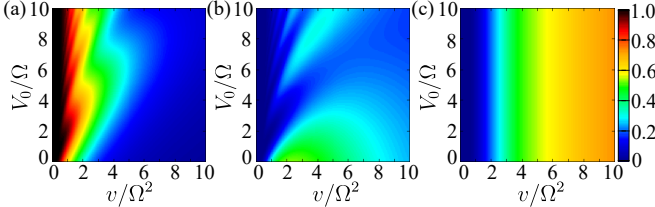


Figure 6. The final population $[P_j(t_f)]$ in (a) $|1\rangle$, (b) $|2\rangle$ and (c) $|3\rangle$, after the linear quench across avoided level crossings, as a function of v and V_0 for the initial state $|\psi(t=0)\rangle = |1\rangle$. We choose the initial time t_i such that $\Delta(t_i) = -10\Omega$, and the final time is such that the populations in the adiabatic states become steady. In the limit $t \rightarrow \infty$, P_1 , P_2 , and P_3 are same as the populations in the diabatic states, i.e., (a) P_{rr} , (b) P_s and (c) P_{gg} respectively.

be sufficiently large, the channel through which the state $|3\rangle$ is populated from $|1\rangle$ via $|2\rangle$ can be visualized. The first population transfer from $|1\rangle$ to $|2\rangle$ takes place around $t = 0$. Since ΔE_0 saturates to a maximum value of $\sqrt{2}\Omega$ as a function of V_0 [see Fig. 4(c)], the magnitude of $P_2(t)$ after the first LZT becomes independent of V_0 for large V_0 and depends only on v . At the same time, $\Delta E_{V_0/2}$ decreases and becomes significantly small ($\Delta E_{V_0/2} \ll \Omega$) at large V_0 . The latter assures a complete non-adiabatic transition from $|2\rangle$ to $|3\rangle$ at the second LZT for sufficiently large v . Also, the transition becomes sharper and sharper in time [see the dashed-dotted line in Figs. 5(h) and 5(i)]. All of the above features make $P_3(t \rightarrow \infty)$ becomes independent of V_0 at sufficiently large V_0 and solely determined by v [see Fig. 6(c)]. Counter-intuitively, even for small V_0 , we

find that $P_3(t \rightarrow \infty)$ is independent of V_0 , and this feature can be better explained using the dynamics in the diabatic basis (see below).

The final populations $P_j(t \rightarrow \infty)$ as a function of v and V_0 are shown in Fig. 6. For $v \ll \Omega^2$ and independent of V_0 , we have $P_1 \sim 1$ [Fig. 6(a)] and $P_{2,3} \sim 0$ [Fig. 6(b) and 6(c)] due to the adiabatic evolution, as mentioned before. In the other extreme limit, $v \gg \Omega^2$, most of the population gets transferred to $|3\rangle$ from $|1\rangle$. For intermediate v , we have patterns in P_1 and P_2 , which are attributed to the interference of LZTs at different instants. Note that, in the limit $t \rightarrow \infty$, P_1 , P_2 , and P_3 are the same as the populations in the diabatic states, i.e., P_{rr} , P_s , and P_{gg} respectively, and so the results in Fig. 6 also show the population in the diabatic states.

Diabatic basis. Experimentally, it is more feasible to measure the populations P_α in the diabatic basis $\alpha \in \{|gg\rangle, |s\rangle, |rr\rangle\}$ directly. In Fig. 7, we show the population dynamics in the diabatic basis for the same dynamics shown in Fig. 5. Since in the limit $t \rightarrow \pm\infty$ both diabatic and adiabatic basis converge, we have $P_{gg}(t \rightarrow -\infty) \sim 1$. Unlike that of adiabatic basis states, the populations in diabatic basis states exhibit clear oscillations (akin to Rabi oscillations) with the amplitude being damped over the relaxation time [see Fig. 7] [85]. The frequency of these oscillations increased over time since the effective instantaneous Rabi frequency increases with an increase in the detuning. For small values of V_0 and v , the amplitude of oscillation is found to be larger. The reason is two-fold, first, for small V_0 , the three LZTs are closely placed, and second, at small v , the system spends more time in the impulse regime. In the adiabatic limit ($v \ll \Omega^2$), all the population is finally transferred to the $|rr\rangle$ state independent of the value of

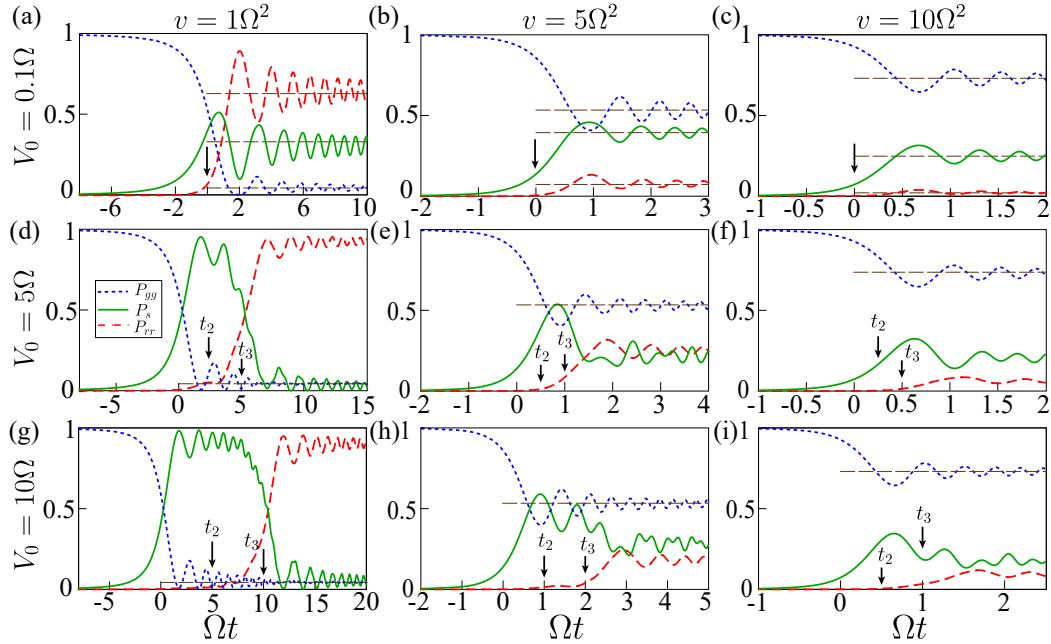


Figure 7. The dynamics of the population in the diabatic states for the initial state $|\psi(t_i)\rangle = |1\rangle$ with different values of v and V_0 . The dashed, solid, and dotted-dashed lines show the populations in states $|gg\rangle$, $|s\rangle$ and $|rr\rangle$ respectively. The thin arrows indicate the times around which the second (t_2) and the third (t_3) LZTs occur. In (a)-(c), the LZTs are not resolvable, so a single arrow is shown. The first LZT occurs in the vicinity of $t = 0$. The dashed horizontal lines are the results of the non-interacting model ($V_0 = 0$). For small V_0 , the latter works very well with all the three states, especially for $|gg\rangle$ even at sufficiently large interaction strengths.

V_0 [see Fig. 6]. For $v \sim \Omega^2$, [along the first column in Fig. 7], independently the value of V_0 , the initial population in $|gg\rangle$ is almost completely transferred into both $|s\rangle$ and $|rr\rangle$, with more population in $|rr\rangle$. As v gets larger and larger, the transition probabilities between the diabatic states get suppressed, reducing the final population in $|s\rangle$ and $|rr\rangle$.

Small V_0 . For $V_0 \ll \Omega$, independent of v , the population transfer to states $|s\rangle$ and $|rr\rangle$ take place near $\Delta \sim 0$ [or $t \sim 0$, see the first row in Fig. 7 for $V_0 = 0.1\Omega$]. The interaction (V_0) is only relevant when Δ is comparable to or smaller than V_0 . At large values of Δ we can ignore the interaction, i.e., away from the avoided crossings. Also, for sufficiently large values of v , the system does not spend significant time within the region of avoided crossings making the effect of interactions minimal. In short, when $V_0/\sqrt{v} \ll 1$, we can approximate the atoms to be non-interacting and use the results from the single atom case for P_{LZ} given in Eq. (3). That gives us, $P_3(t \rightarrow \infty) = P_{gg} \sim P_{LZ}^2$, $P_2(t \rightarrow \infty) = P_s \sim 2P_{LZ}(1 - P_{LZ})$ and $P_1(t \rightarrow \infty) = P_{rr} \sim (1 - P_{LZ})^2$ in the limit $t \rightarrow \infty$ and are shown by dashed horizontal lines in the first row of Fig. 7. They are found to be in good agreement with the numerical results. As v becomes larger and larger, P_{LZ} gets augmented, making $P_{rr}(t \rightarrow \infty)$ smaller and smaller compared to $P_{gg}(t \rightarrow \infty)$ and $P_s(t \rightarrow \infty)$. Keeping V_0 small, and for sufficiently large values of V_0/\sqrt{v} , based on scaling arguments and the insights from the numerical results, we can approximately write down the final populations as $P_{gg} \sim P_{LZ}^2$ [unchanged from the non-interacting model, see Fig. 6(c)],

$$P_s \sim 1 - P_{LZ}^2 - (1 - Q_{LZ})^2, \quad (17)$$

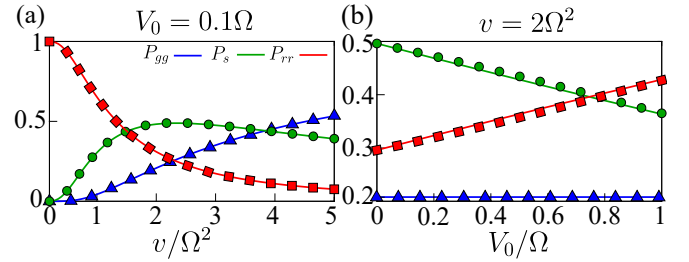


Figure 8. (a) The final $[P_j(t \rightarrow \infty)]$ population in the adiabatic states as a function of v for $V_0 = 0.1\Omega$ and the initial state $|1\rangle$. (b) The same as in (a) but as a function of V_0 and for $v = 2\Omega^2$. The solid lines are from the exact numerical calculations, and the filled squares, circles, and triangles are the theoretical prediction for small V_0 given in Eq. (17) for the states $P_1(t \rightarrow \infty) = P_{rr}$, $P_2(t \rightarrow \infty) = P_s$, and $P_3(t \rightarrow \infty) = P_{gg}$, respectively.

and $P_{rr} \sim (1 - Q_{LZ}^2)$ where

$$Q_{LZ} = P_{LZ} \exp\left(-\frac{\pi\Omega^2 V_0}{4v^{3/2}}\right). \quad (18)$$

These results are in excellent agreement with the exact numerical results [see Fig. 8] even for sufficiently large values of V_0 . Also, Eqs. (17) and (18) reveal that there are no interference effects on the final population from distinct LZTs for small V_0 since the different LZTs are not separable.

Large V_0 . Using the population dynamics in the adiabatic basis states, we have shown that when V_0 is large, and for

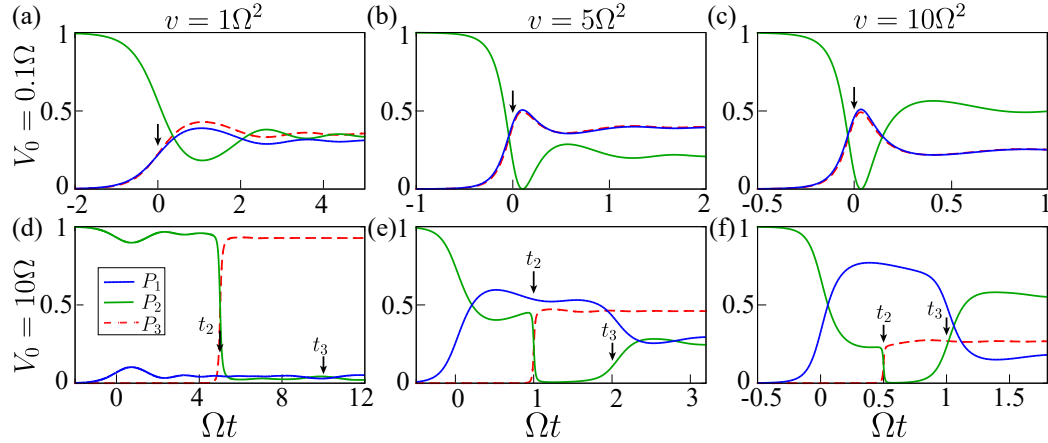


Figure 9. The dynamics of the population in the adiabatic states for the initial state $|\psi(t_i)\rangle = |2\rangle$ with different values of v and V_0 . The dashed, solid, and dotted-dashed lines show the populations in states $|1\rangle$, $|2\rangle$, and $|3\rangle$ respectively. The thin arrows indicate the times around which the second (t_2) and the third (t_3) LZTs occur. In (a)-(c), the LZTs are not resolvable, so a single arrow is shown. The first LZT occurs in the vicinity of $t = 0$.

intermediate values of v , we can distinguish the three different LZTs [see second and third rows in Fig. 5]. But this is only partially possible using the dynamics of the diabatic basis states. The reason is that $|gg\rangle$ is not directly coupled to $|rr\rangle$ leaving no sign of second LZT (around t_2) in the dynamics [see Figs. 7(d) and 7(g)]. In the vicinity of the first LZT ($t = 0$), the states $|gg\rangle$ and $|s\rangle$ get admixed, resulting in a decrease in $P_{gg}(t)$, and an increment in $P_s(t)$ as seen in Fig. 7. If v is sufficiently small, almost a complete transfer from $|gg\rangle$ to $|s\rangle$ takes place. As $\Delta(t)$ approaches the third LZT at t_3 , we again have a population transfer, from state $|s\rangle$ to $|rr\rangle$. That means, for $V_0/v \gg 1/\Omega$, essentially the system evolves from an uncorrelated state ($|gg\rangle$), and pass through an entangled state ($|s\rangle$) and eventually end up in an uncorrelated doubly excited state ($|rr\rangle$). Thus, an adiabatic evolution is guaranteed by the criteria $V_0/v \gg 1/\Omega$ if the initial state is $|gg\rangle$ or $|1\rangle$. The duration in which the system stays in each of these states can be controlled by the fine-tuning of v and V_0 . From the above analysis, we could extract out an interesting fact on $P_{gg}(t \rightarrow \infty)$. For small V_0 , we have $P_{gg} \sim P_{LZ}^2$ from the non-interacting model, and at the same time, we know that $P_3(t \rightarrow \infty) = P_{gg}(t \rightarrow \infty)$ is independent of V_0 [see Fig. 6]. That means, independent of the value of V_0 , we have $P_{gg}(t \rightarrow \infty) = P_{LZ}^2$ a result from the non-interacting model. But such a simplified result ceases to exist for $|s\rangle$ and $|rr\rangle$ states at sufficiently large V_0 . A simple inspection based on the diabatic basis can be used to understand why $P_3(t \rightarrow \infty)$ or $P_{gg}(t \rightarrow \infty)$ is independent of V_0 if the initial state is $|1\rangle \sim |gg\rangle$. The state $|gg\rangle$ is coupled only to $|s\rangle$, and V_0 should play no role in determining how much population transfer occurs from $|gg\rangle$ to $|s\rangle$ since two excitations are not involved in the process. But V_0 can affect the population transfer from $|s\rangle$ to $|gg\rangle$ since $|s\rangle$ couple to $|rr\rangle$ also. Therefore, for the single sweep across the avoided crossings, $P_{gg}(t \rightarrow \infty)$ is independent of V_0 . As we see later, the same would be true for $P_1(t \rightarrow \infty)$ or $P_{rr}(t \rightarrow \infty)$ if the initial state is $|rr\rangle$.

2. $|\psi(t_i)\rangle = |2\rangle$

At this point, we briefly comment on the adiabaticity of the evolution with different initial states. When the initial state is $|1\rangle$ and for sufficiently large V_0 , the gap $\Delta E_0 \sim \sqrt{2}\Omega$ (same as ΔE_{V_0}) set the adiabatic limit, which becomes independent of V_0 . But, if the initial state is either $|2\rangle$ or $|3\rangle$, the adiabatic limit is set by the inverse of the gap, $\Delta E_{V_0/2}$ (smallest among the three gaps), which decreases monotonously with an increase in V_0 as seen in Fig. 4(c). Therefore, for large V_0 , at $\Delta(t) = V_0/2$, there is a significant population transfer between the states $|2\rangle$ and $|3\rangle$ unless v is negligibly small. In short, a significantly large value of V_0/v may not guarantee an adiabatic evolution if the initial state is $|2\rangle$ or $|3\rangle$. For $V_0 \gg \Omega$, approximating each avoided level crossings composed of only two levels and using the adiabatic theorem, we require $v \ll 2\Omega^2$ for an adiabatic evolution with the initial state $|1\rangle$. Similarly, we need $v \ll 4\Omega^4/V_0^2$ for an adiabatic evolution with the initial state $|2\rangle$ or $|3\rangle$.

Adiabatic basis. Fig. 9 shows the population dynamics in the adiabatic basis for the initial state $|2\rangle$. For $V_0 \ll \Omega$ and sufficiently large v , as we have shown before, the interaction V_0 will be irrelevant in the dynamics. In that case, the population dynamics of both $|1\rangle$ and $|3\rangle$ become identical [see Figs. 9(b) and 9(c)]. When v is sufficiently small, V_0 becomes relevant, and that symmetry is lost in the dynamics as seen in Fig. 9(a), i.e., $P_1(t) \neq P_3(t)$. As we did before, when V_0 is sufficiently large, we understand the dynamics analyzing individual LZTs. Near $t = 0$, the population in $|2\rangle$ gets transferred to $|1\rangle$, and larger the value of v , stronger the non-adiabatic transition between them [see Figs. 9(d)-9(f)]. In the vicinity of the second LZT (t_2), almost a complete transfer from $|2\rangle$ to $|3\rangle$ occurs for sufficiently large v due to the tiny energy gap. That leaves a negligible or vanishing population in state $|2\rangle$ after the second LZT. But, near t_3 when the system crosses the third LZT, the state $|2\rangle$ gains population from $|1\rangle$. The population mostly transfer from $|1\rangle$ to $|2\rangle$ at the third LZT. That makes the final

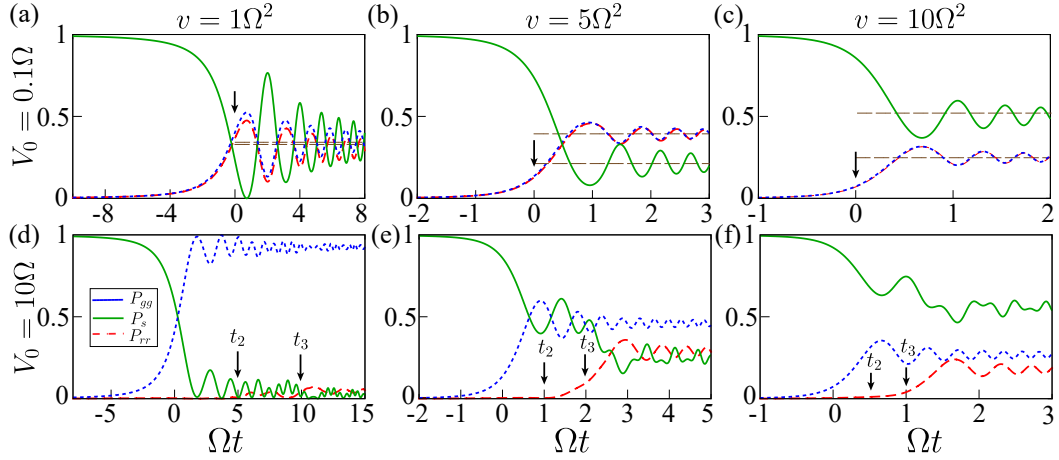


Figure 10. The dynamics of the population in the diabatic basis for different values of v and V_0 for the initial state $|\psi(t_i)\rangle = |2\rangle$. The dashed, solid, and dotted-dashed lines show the populations in states $|gg\rangle$, $|s\rangle$ and $|rr\rangle$ respectively. The horizontal lines in (a)-(c) show the results from the non-interacting LZ model. The thin arrows indicate the times around which the second (t_2) and the third (t_3) LZTs occur. In (a)-(c), the LZTs are not resolvable, so a single arrow is shown. The first LZT occurs in the vicinity of $t = 0$.

population in $|2\rangle$ becomes larger and larger with an increase in v at large v whereas that of $|1\rangle$ and $|3\rangle$ decreases. Also, as V_0 becomes larger and larger, the second LZT at t_2 becomes sharper and sharper.

Diabatic basis. In Fig. 10, we show the population dynamics in the diabatic basis for the same dynamics shown in Fig. 9. We have an initial state such that $P_s \sim 1$. The population in $|s\rangle$ gets transferred to $|gg\rangle$ and $|rr\rangle$ states symmetrically for small V_0 and large v , as seen in Figs. 10(b) and 10(c) because V_0 is irrelevant at large velocities. This symmetry is lost as v becomes smaller, identical to what we have discussed regarding the populations in the adiabatic basis. For the initial state $|2\rangle$, the results obtained from the non-interacting LZ model are $P_{gg}(t \rightarrow \infty) = P_{rr}(t \rightarrow \infty) \sim 2P_{LZ}(1 - P_{LZ})$, and $P_s(t \rightarrow \infty) \sim 1 - 4P_{LZ}(1 - P_{LZ})$, which have been shown as horizontal lines in Fig. 10(a)-10(c) that are valid at small V_0 and sufficiently large v or when $V_0/\sqrt{v} \ll 1$. Incorporating the finite V_0 , using the scaling arguments together with symmetry requirement of LZT matrix, we arrive at,

$$P_1(t \rightarrow \infty) = P_{rr} \sim 1 - P_{LZ}^2 - (1 - R_{LZ})^2, \quad (19)$$

$$P_3(t \rightarrow \infty) = P_{gg} \sim 1 - P_{LZ}^2 - (1 - Q_{LZ})^2, \quad (20)$$

where

$$R_{LZ} = P_{LZ} \exp\left(-\frac{\pi\Omega^2 V_0}{2^{5/2} v^{3/2}}\right),$$

and $P_2(t \rightarrow \infty) = P_s = 1 - P_{rr} - P_{gg}$. These results are found to be in excellent agreement with numerical results (not shown). If V_0 is sufficiently large, near $t = 0$, first, we have a population transfer from $|s\rangle$ to $|gg\rangle$ [see Figs. 10(d)-10(f)]. Besides, if v is sufficiently small (provided by the adiabatic criteria), we have almost a complete transfer of population to $|gg\rangle$. The second LZT is inactive, as $|gg\rangle$ and $|rr\rangle$ are not coupled. Therefore $P_{gg}(t)$ remains unchanged as $t \rightarrow \infty$, leaving no sign of second and third LZTs in the dynamics. There is an interesting catch, one would expect more excitations to be

created by sweeping detuning from negative to large positive values [104–106], but as we explicitly show it indeed depends on the initial conditions and the nature of the associated level crossings. Here, we dynamically de-excited a two atom-setup completely [see Fig. 10(d)] starting from a partially excited state (a collective single excitation state). If both V_0 and v are sufficiently large, a transfer of population from $|s\rangle$ to $|gg\rangle$ occurs only partially. Across the third LZT point (t_3), the population from $|s\rangle$ gets transferred to $|rr\rangle$.

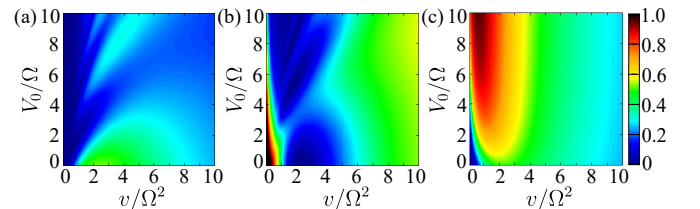


Figure 11. The final population in the adiabatic (diabatic) basis: (a) $|1\rangle$ ($|rr\rangle$), (b) $|2\rangle$ ($|s\rangle$) and (c) $|3\rangle$ ($|gg\rangle$) as a function of v and V_0 for the initial state $|\psi(t_i)\rangle = |2\rangle$. We choose the initial time t_i such that $\Delta(t_i) = -10\Omega$, and the final time is such that the populations in the adiabatic states become steady. In the limit $t \rightarrow \infty$, P_1 , P_2 , and P_3 are the same as the populations in the diabatic states, i.e., (a) P_{rr} , (b) P_s , and (c) P_{gg} , respectively.

The above dynamics have been summarized with density plots for the final populations as a function of v , and V_0 [see Fig. 11] for the initial state $|2\rangle$. One of the main differences from the results in Fig. 6(d) using the initial state $|1\rangle$ is that of the initial condition $|2\rangle$, the final population $P_3(t \rightarrow \infty)$ or $P_{gg}(t \rightarrow \infty)$ is no longer independent of V_0 [see Fig. 11(c)]. As it is clear, for small v and V_0 , the population almost remain in state $|2\rangle$ indicating an adiabatic evolution. The adiabaticity is quickly lost as soon as V_0 gets larger due to the smallness of $\Delta E_{V_0/2}$. Therefore, at large V_0 , even for relatively small v , across the second LZT (t_2), the population gets mostly trans-

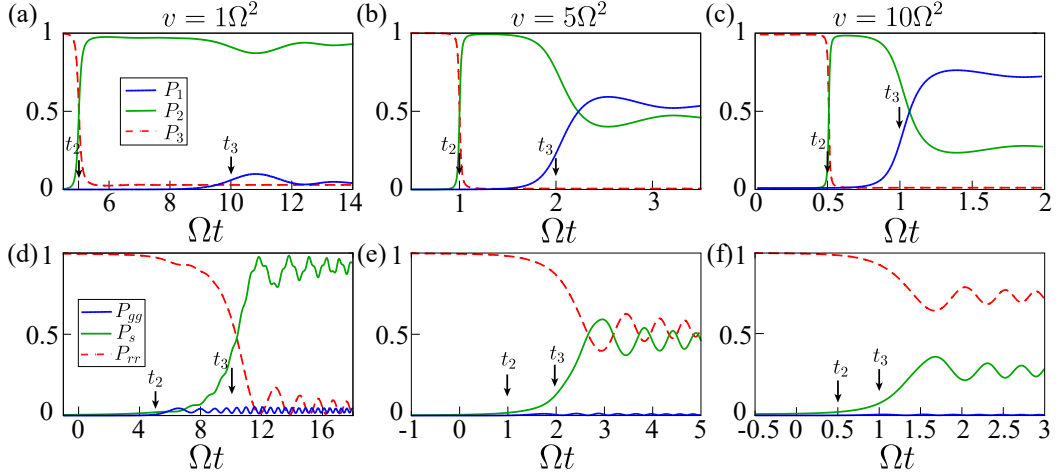


Figure 12. The dynamics of population in the adiabatic (a)-(c) and diabatic (d)-(f) states for the initial state $|\psi(t_i)\rangle = |3\rangle$ with different values of v and $V_0 = 10\Omega$. The dashed, solid, and dotted-dashed lines show the populations in states $|1\rangle$ ($|gg\rangle$), $|2\rangle$ ($|s\rangle$), and $|3\rangle$ ($|rr\rangle$) respectively. The thin arrows show the times around which the second (t_2) and the third (t_3) LZTs occur.

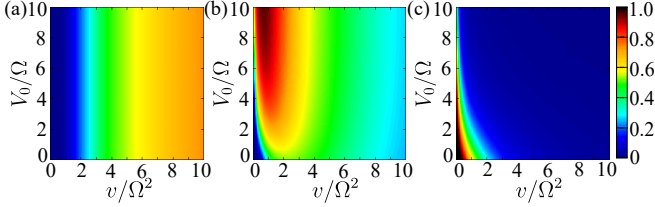


Figure 13. The final population in the adiabatic (diabatic) basis: (a) $|1\rangle$ ($|rr\rangle$), (b) $|2\rangle$ ($|s\rangle$) and (c) $|3\rangle$ ($|gg\rangle$) as a function of v and V_0 for the initial state $|\psi(t_i)\rangle = |3\rangle$. The solid, dashed and dotted-dashed lines show the populations in states $|1\rangle$, $|2\rangle$, and $|3\rangle$ respectively.

ferred to the state $|3\rangle$. That makes $P_3(t \rightarrow \infty)$ or $P_{gg}(t \rightarrow \infty)$ being different at small and large values of V_0 . Fixing V_0 to a large value, and varying v , we see that $P_3(t \rightarrow \infty)$ first increases reaches a maximum and then monotonously decreases [see Fig. 11(c)]. The initial increase in $P_3(t \rightarrow \infty)$ with v is attributed to the smallness of $\Delta E_{V_0/2}$, whereas at large values of v , around the first avoided crossing the population $P_2(t)$ increasingly gets transferred to $|1\rangle$ resulting in a decrease in $P_3(t \rightarrow \infty)$. The latter effectively increases the population $P_2(t \rightarrow \infty)$ across the third LZT at the cost of $|1\rangle$ and $|3\rangle$ at large V_0 and v . Note that, interference of different LZTs lead to non-trivial patterns in $P_1(t \rightarrow \infty)$ and $P_2(t \rightarrow \infty)$ as a function of v and V_0 [see Fig. 11(a) and 11(b)].

3. $|\psi(t_i)\rangle = |3\rangle$

Adiabatic basis. In contrary to the dynamics for which the initial state is $|1\rangle$ or $|2\rangle$, here, the first avoided crossing becomes completely irrelevant at large V_0 . Hence, for large V_0 , the population transfer first occurs in the vicinity of t_2 , from $|3\rangle$ to $|2\rangle$. Since $\Delta E_{V_0/2}$ is very small at large V_0 , a sufficiently large v leads to a complete transfer from $|3\rangle$ to $|2\rangle$, as seen in Figs. 12(a)-12(c). Then, near the third avoided crossing

($t \sim t_3$), we have a population transfer from $|2\rangle$ to $|1\rangle$. And, larger the value of v larger the non-adiabatic transition to $|1\rangle$. Thus, for sufficiently large values of V_0 and v , we do not find any population in P_3 at $t \rightarrow \infty$ [see Figs. 12(c) and 13(c)].

Diabatic basis. The dynamics of the populations in the diabatic basis for the initial state $|3\rangle$ (or equivalently $|rr\rangle$ in the limit $t \rightarrow -\infty$) are shown in Fig. 12(d)-12(f). Note that $|rr\rangle$ is not coupled to $|gg\rangle$, it implies that the population can only transfer to $|s\rangle$. For large V_0 , the latter only occurs across the third LZT ($t \sim t_3$). Therefore the dynamics in the diabatic basis are characterized by only a single transition (population transfer) over the entire time evolution. And, larger the value of v , the weaker the transition between $|rr\rangle$ and $|s\rangle$. For small V_0 and large v , we can use the results from the non-interacting LZ model: $P_{rr} \sim P_{LZ}^2$, $P_s \sim 2P_{LZ}(1 - P_{LZ})$, and $P_{gg} \sim (1 - P_{LZ})^2$ obtained for the initial state $|3\rangle \sim |rr\rangle$. By including the effect of a finite and small V_0 , we have $P_3(t \rightarrow \infty) = P_{gg} \sim (1 - R_{LZ})^2$, $P_2(t \rightarrow \infty) = P_s \sim 1 - P_{LZ}^2 - (1 - R_{LZ})^2$, and $P_1(t \rightarrow \infty) = P_{rr} \sim P_{LZ}^2$.

The final population in the adiabatic or diabatic basis as a function of v and V_0 for the initial state $|3\rangle$ is shown in Fig. 13. As discussed above, for large V_0 and v , we have $P_3(t \rightarrow \infty) = P_{gg} \sim 0$. In the adiabatic limit (both V_0 and v are very small), we have $P_3(t \rightarrow \infty) \sim 1$. Fixing V_0 to a large value, and varying v , we see that $P_2(t \rightarrow \infty)$ first increases reaches a maximum and then monotonously decreases [see Fig. 13(b)]. This non-monotonous behaviour of $P_2(t \rightarrow \infty)$ can be understood from the nature of the gaps $\Delta E_{V_0/2}$ and ΔE_{V_0} at large V_0 . Since $\Delta E_{V_0/2} \ll \Delta E_{V_0}$, the time evolution at the second avoided crossing is highly non-adiabatic compared to that at the third. That results in the initial increase of $P_2(t \rightarrow \infty)$ as a function of v . At higher values of v , the evolution across the third avoided crossing as well become strongly non-adiabatic, resulting in a decrease of $P_2(t \rightarrow \infty)$ at the cost of P_1 . Another feature is that $P_1(t \rightarrow \infty)$ is independent of V_0 , and again, we use the diabatic basis to explain it. The initial $|rr\rangle$ state is only coupled to $|s\rangle$ state, and the population

transfer between them mostly takes place in the impulsive region, i.e., in the vicinity of $|V_0 - \Delta(t)| \sim 0$ irrespective of the value of V_0 . The latter makes V_0 becomes non-relevant in estimating the transition probability from $|rr\rangle$ to $|s\rangle$. After that, $|rr\rangle$ is not involved in any non-adiabatic transitions, making $P_1(t \rightarrow \infty) \sim P_{rr}$ independent of V_0 .

Comparing the results from the three different initial conditions, we found an interesting pattern that the probability distribution in the $v - V_0$ plane for the final populations are repeating. Each initial state provides us three patterns and hence, a total of nine. But out of which only six are distinct from each other. The identical patterns are (i) $P_3(t \rightarrow \infty)$ with initial state $|1\rangle$ and $P_1(t \rightarrow \infty)$ with initial state $|3\rangle$, (ii) $P_2(t \rightarrow \infty)$ with initial state $|1\rangle$ and $P_1(t \rightarrow \infty)$ with initial state $|2\rangle$ and (iii) $P_3(t \rightarrow \infty)$ with initial state $|2\rangle$ and $P_2(t \rightarrow \infty)$ with initial state $|3\rangle$.

4. Beats

Two interesting features previously found in the study of a triangular LZ model, depending on the geometric size of the triangle formed by the three avoided crossings [see Fig. 4(b)], are the beats and step patterns in the population dynamics of the diabatic basis [9, 81]. These patterns arise due to the quantum interference of distinct LZTs. We only briefly comment on the beats pattern in our setup. The beats pattern is observed only in the population of the $P_s(t)$ and that for two different initial conditions are shown in Fig. 14(a). Based on the calculations discussed for the triangular LZ model in Ref. [9], we would expect a beat pattern in $P_s(t)$ if $\Omega^2/4v \ll 1$ and $V_0^2/4v < 1$. The envelope frequency is found to be $V_0/2$, and the fast oscillation frequency changes over time as approximately $vt/4$.

5. AIA

In this section, we employ AIA for analyzing the dynamics for the linear quench of the detuning across the three LZTs. For sufficiently large values of interactions ($V_0 > \sqrt{2}\Omega$), the three avoided level crossings can be made isolated [see Figs. 4(b) and 14(b)]. That helps us to identify adiabatic and impulsive regimes. Further, we approximate that, across each avoided crossings, only two adiabatic states are involved. The latter allows us to use the results from the two-level LZ model discussed in Sec. I. To implement AIA, we require LZT time (τ_{LZ}) should be shorter than the duration ($T_a = V_0/2v$) in which the system undergoes adiabatic evolution between two LZTs. Since $\Delta E_0 = \Delta E_{V_0} > \Delta E_{V_0/2}$ for $V_0 \neq 0$, we only need to compare the LZT time across the first avoided crossing with T_a . The former has an upper limit set by $\tau_{LZ} \approx (1/2\sqrt{v})\max(1, \Omega^2/2v)$ [84]. Therefore, for $v > \Omega^2/2$, we require $V_0^2 > v$ and for $v < \Omega^2/2$, we require $16V_0^2/\Omega^4 > v$ for AIA to be valid. The adiabatic evolution matrix [see Fig.

14(b)] in the adiabatic basis $\{|3\rangle, |2\rangle, |1\rangle\}$, is given by

$$\hat{U}_k = \begin{pmatrix} e^{-i\zeta_3^{(k)}} & 0 & 0 \\ 0 & e^{-i\zeta_2^{(k)}} & 0 \\ 0 & 0 & e^{-i\zeta_1^{(k)}} \end{pmatrix},$$

where $\zeta_j^{(1)} = \int_{t_1}^{t_1} dt E_j$, $\zeta_j^{(2)} = \int_{t_1}^{t_2} dt E_j$, $\zeta_j^{(3)} = \int_{t_2}^{t_3} dt E_j$, and $\zeta_j^{(4)} = \int_{t_3}^{t_f} dt E_j$ are the phases acquired between different avoided crossings. The non-adiabatic transition matrices $\hat{G}1_{LZ}$, $\hat{G}2_{LZ}$, and $\hat{G}3_{LZ}$ at the impulse points t_1 , t_2 , and t_3 , respectively are found to be, in the adiabatic basis $\{|3\rangle, |2\rangle, |1\rangle\}$

$$\hat{G}1_{LZ} = \begin{pmatrix} 1 & 0 & 0 \\ 0 & \sqrt{1 - P'_{LZ}} e^{-i\tilde{\phi}'_s} & -\sqrt{P'_{LZ}} \\ 0 & \sqrt{P'_{LZ}} & \sqrt{1 - P'_{LZ}} e^{i\tilde{\phi}'_s} \end{pmatrix} \quad (21)$$

where $P'_{LZ} = \exp(-2\pi\Omega'^2/4v)$, and

$$\tilde{\phi}'_s = \pi/4 + \arg(\Gamma(1 - iy')) + y'(\ln y' - 1) \quad (22)$$

with $y' = \Omega'^2/4v$ and $\Omega' = \Delta E_0 \sim \sqrt{2}\Omega$. The transition matrix at t_2 is

$$\hat{G}2_{LZ} = \begin{pmatrix} \sqrt{1 - P''_{LZ}} e^{-i\tilde{\phi}''_s} & -\sqrt{P''_{LZ}} & 0 \\ \sqrt{P''_{LZ}} & \sqrt{1 - P''_{LZ}} e^{i\tilde{\phi}''_s} & 0 \\ 0 & 0 & 1 \end{pmatrix} \quad (23)$$

with $P''_{LZ} = \exp(-2\pi\Omega''^2/8v)$ and

$$\tilde{\phi}''_s = \pi/4 + \arg(\Gamma(1 - iy'')) + y''(\ln y'' - 1) \quad (24)$$

with $y'' = \Omega''^2/8v$ and $\Omega'' = \Delta E_{V_0/2}$. It can be easily seen that we have $\hat{G}1_{LZ} = \hat{G}3_{LZ}$ since at t_3 , again $|1\rangle$ and $|2\rangle$ are only involved in the transition. Thus, for sufficiently large values of V_0 and within the AIA, the complete evolution matrix for a linear quench across all the three LZTs is given by $\hat{F}_L = \hat{U}_4 \hat{G}3_{LZ} \hat{U}_3 \hat{G}2_{LZ} \hat{U}_2 \hat{G}1_{LZ} \hat{U}_1$. The results from AIA are compared to that of exact numerics and are shown in Fig. 16, for different initial conditions. They are in excellent agreement even for parameter values beyond the criteria we have discussed above. One of the reasons could be that τ_{LZ} only sets the upper limit for the transition time, but the real transition time can be significantly shorter than τ_{LZ} especially, at large values of v . As shown in Figs. 16(a) and 16(c), for a fixed v , the final population in states $|s\rangle$ and $|rr\rangle$ exhibits oscillations as a function of V_0 , indicating the role of quantum interference between the distinct LZTs. On the other hand, for a fixed V_0 , and varying v , we do not observe any oscillations. It indicates that the Stokes phases ($\tilde{\phi}'_s$ and $\tilde{\phi}''_s$) become irrelevant in the final populations if the initial state is one of the instantaneous eigenstates. We have verified this by setting $\tilde{\phi}'_s = \tilde{\phi}''_s = 0$ in the matrices $\hat{G}1_{LZ}$ and $\hat{G}2_{LZ}$, and the results are hardly affected by it. If the initial state is a superposition of the adiabatic basis states, the Stokes phases become important. In that case, we will be able to observe oscillations in the populations $[P_j(t \rightarrow \infty)]$ as a function of v keeping V_0 fixed.

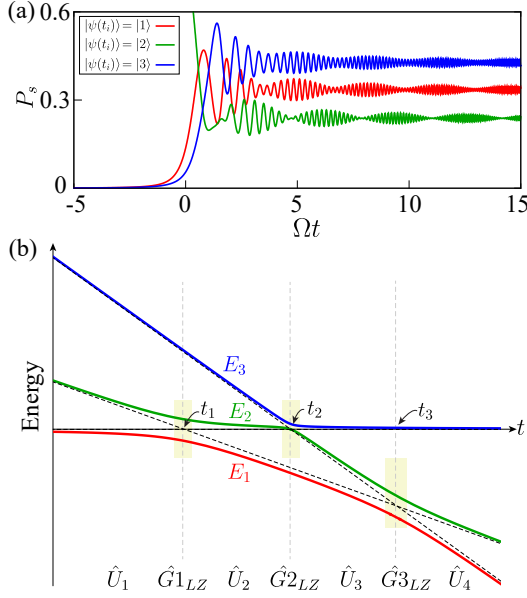


Figure 14. (a) The formation of beats in the dynamics of $P_s(t)$ for different initial conditions with $V_0 = 2\Omega$ and $v = 5\Omega^2$ under a linear quench of detuning from a far negative to a far positive value, involving all three avoided crossings. (b) The adiabatic (\hat{U} 's) and non-adiabatic ($\hat{G}1_{LZ}$, $\hat{G}2_{LZ}$, $\hat{G}3_{LZ}$) regimes as a function of time for $\Delta(t) = vt$ and $V_0 \gg \Omega$. The times t_1 , t_2 , and t_3 are the times at which the system crosses the first, second, and third avoided level crossings, respectively. E_1 , E_2 , and E_3 are the instantaneous eigenenergies.

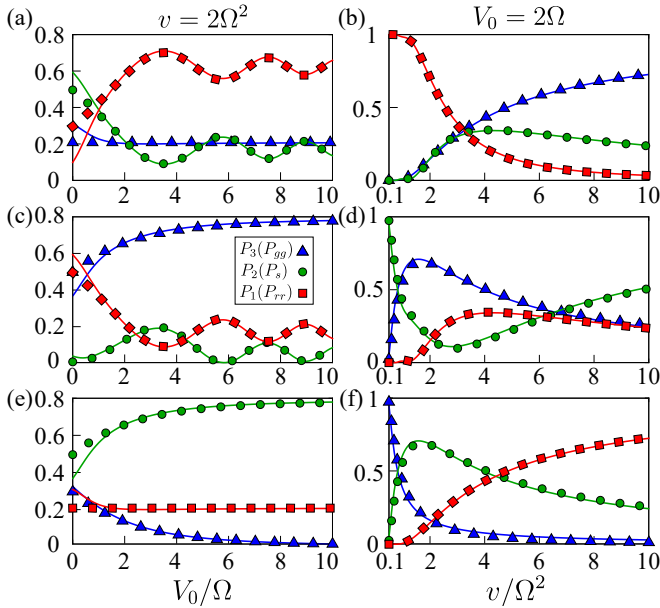


Figure 15. The final $[P_j(t \rightarrow \infty)]$ population in the adiabatic (diabatic) states as a function of V_0 for the initial state (a) $|1\rangle$, (c) $|2\rangle$, and (e) $|3\rangle$ with $v = 2\Omega^2$. The same as a function of v for the initial state (b) $|1\rangle$, (d) $|2\rangle$, and (f) $|3\rangle$ with $V_0 = 2\Omega$. The solid lines are the results from the exact numerics, and the filled squares, circles, and triangles are from the AIA for the states $P_1(t \rightarrow \infty) = P_{rr}$, $P_2(t \rightarrow \infty) = P_s$ and $P_3(t \rightarrow \infty) = P_{gg}$, respectively. As seen in (a), (c), and (e), for sufficiently large V_0 , the results from AIA are in excellent agreement with the exact numerical results.

B. Periodic modulation of detuning

Now, we consider the detuning is varying periodically in time as $\Delta(t) = \Delta_0 + \delta \sin(\omega t)$. We take $V_0 \gg \Omega$ and $\Delta_0 \ll 0$. The first condition assures that the three avoided level crossings are well separated, and we can implement AIA, as discussed in Sec. III A 5. The second condition guarantees us that the adiabatic states converge to the diabatic ones far left to the first avoided level crossing. The initial offset in detuning (Δ_0) is crucial in determining the final populations in the diabatic or adiabatic states. Because Δ_0 affects the dynamical phases accumulated during the adiabatic evolutions between the LZTs. Here, we analyze the dynamics as a function of δ and ω_0 for the three different initial states. Henceforth, we set the initial time $t = t_i = 0$. As we have mentioned before, the three distinct avoided crossings occur at $\Delta(t) = 0$, $\Delta(t) = V_0/2$ and $\Delta(t) = V_0$. To determine the quench rate of the detuning across the avoided crossings, we linearize $\Delta(t) = \Delta_0 + \delta \sin \omega t$ in time within the vicinity of the instants at which the avoided crossings take place. The first avoided crossing (involving states $|1\rangle$ and $|2\rangle$) occurs when $\Delta(t) = 0$, i.e., at times $\tau_{2n}^{(1)} = [2n\pi + \sin^{-1}(-\Delta_0/\delta)]/\omega$ and $\tau_{2n+1}^{(1)} = [(2n+1)\pi - \sin^{-1}(-\Delta_0/\delta)]/\omega$ with $n = 0, 1, 2, \dots$. Now, linearizing around $\tau_m^{(1)}$, i.e., $\Delta(\tau_m^{(1)} + t) = \Delta_0 + \delta \sin \omega(\tau_m^{(1)} + t) \approx \delta \omega t \cos \omega \tau_m^{(1)} = (-1)^m \omega \sqrt{\delta^2 - \Delta_0^2} t$, we obtain the quench rate as $v_1 = \pm \omega \sqrt{\delta^2 - \Delta_0^2}$. Similarly, the second avoided crossing (involving states $|2\rangle$ and $|3\rangle$) occurs when $\Delta(t) = V_0/2$ or at $\tau_{2n}^{(2)} = [2n\pi + \sin^{-1}((V_0/2 - \Delta_0)/\delta)]/\omega$ and $\tau_{2n+1}^{(2)} = [(2n+1)\pi - \sin^{-1}((V_0/2 - \Delta_0)/\delta)]/\omega$, and the third avoided crossing (again involving states $|1\rangle$ and $|2\rangle$) occurs when $\Delta(t) = V_0$ or at $\tau_{2n}^{(3)} = [2n\pi + \sin^{-1}((V_0 - \Delta_0)/\delta)]/\omega$ and $\tau_{2n+1}^{(3)} = [(2n+1)\pi - \sin^{-1}((V_0 - \Delta_0)/\delta)]/\omega$. The corresponding quench rates are obtained as $v_2 = \pm \omega \sqrt{\delta^2 - (\Delta_0 - V_0/2)^2}$ and $v_3 = \pm \omega \sqrt{\delta^2 - (\Delta_0 - V_0)^2}$, respectively. Appropriately replacing v by v_1 , v_2 , and v_3 , we can use the LZT matrices $\hat{G}1_{LZ}$, $\hat{G}2_{LZ}$, and $\hat{G}3_{LZ}$ to analyze the dynamics within the AIA. Note that, v_1 is different from v_3 which makes $\hat{G}1_{LZ} \neq \hat{G}3_{LZ}$, in contrary to the case of linear quench discussed in Sec. III A 5. Using the quench rates, we estimate the upper limit for the LZT time across the LZTs at $\tau_m^{(1)}$ and $\tau_m^{(3)}$ as $\tau_{LZ1} = 1/\sqrt{|v_1|} \max(1, \Omega'^2/4|v_1|)$ and $\tau_{LZ3} = 1/\sqrt{|v_3|} \max(1, \Omega'''^2/4|v_3|)$, respectively. The LZT time for the one at $\tau_m^{(2)}$ becomes extremely small (almost instant, as evident from the results shown in Sec. III A) at large V_0 . Between two LZTs, the system undergoes an adiabatic evolution.

Based on the value of δ , we restrict the analysis to three different cases. The case (i) is such that the maximum of $\Delta(t)$ lies at the midway between the first ($\Delta = 0$) and second ($\Delta = V_0/2$) avoided crossings (see Fig. 16), i.e., $\delta = V_0/4 - \Delta_0$, (ii) the midway between the second ($\Delta = V_0/2$) and third ($\Delta = V_0$) avoided crossings (see Fig. 16), i.e., $\delta = 3V_0/4 - \Delta_0$. The third one (iii) is with $\delta \gg V_0 - \Delta_0$. In the first case, the system is periodically driven across only the first avoided crossing; in second, both first and second avoided crossings are included,

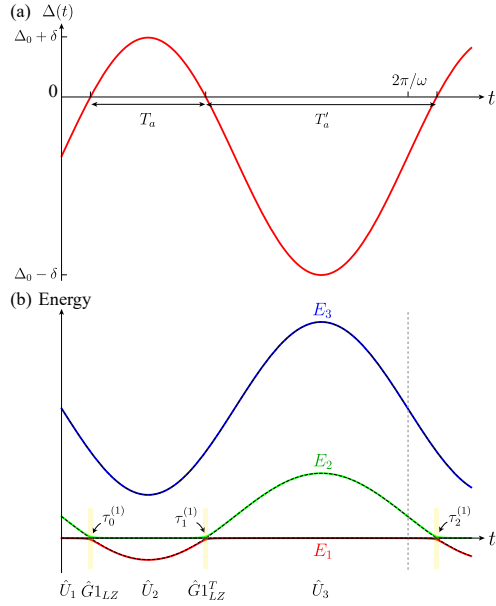


Figure 16. (a) the periodic time dependence of the detuning for $\delta = V_0/4 - \Delta_0$. The durations in which adiabatic evolution takes place in AIA is marked by T_a and T'_a . (b) shows the corresponding instantaneous energy eigenvalues. The instants $(\tau_0^{(1)}, \tau_1^{(1)}, \tau_2^{(1)})$ at which the LZTs occur between states $|1\rangle$ and $|2\rangle$ are shown by shaded stripes. Between each of these LZTs, adiabatic evolution takes place. The \hat{U}_j and $\hat{G}1_{LZ}$ operators are the adiabatic evolution and non-adiabatic transition matrices, respectively. Between the origin and the dashed vertical line, we have one complete cycle.

and in third, all the three of the avoided crossings are involved in the dynamics. As discussed in [64], the periodic driving results in various resonances in the system. For instance, in the high-frequency limit ($\omega \gg \Omega$) or the fast-passage limit ($\omega \sqrt{\delta^2 - \Delta_0^2} \gg \Omega$) a resonant transition between $|gg\rangle$ and $|s\rangle$ takes place when $n\omega = \Delta_0$ with $n = 0, \pm 1, \pm 2, \dots$, resulting in coherent Rabi oscillations between the two states. Similarly, for $n\omega = 2\Delta_0 - V_0$ and $n\omega = \Delta_0 - V_0$, there exists a resonant transition between $|gg\rangle$ and $|rr\rangle$, and $|s\rangle$ and $|rr\rangle$, respectively. The resonant transition between $|gg\rangle$ and $|rr\rangle$ (antiblockades) can takes place via two scenarios: with or without any significant population in $|s\rangle$ state. As one can see from resonance criteria, to resolve different resonances in ω , one requires a large V_0 .

1. $\delta = V_0/4 - \Delta_0$

In this case, the detuning varies periodically across the first level crossing, and the maximum of $\Delta(t)$ is such that it is in midway between the first and the second avoided crossings [see Figs. 14(b) and 16]. The LZT at the first avoided crossing is quantified by the transition matrix $\hat{G}1_{LZ}$ in which the rate v is replaced by v_1 given above. The evolution matrix for one cycle can be written as $\hat{F} = \hat{U}_3 \hat{G}1_{LZ}^T \hat{U}_2 \hat{G}1_{LZ} \hat{U}_1$ [see Fig. 16(b)]. There are three different time scales in-

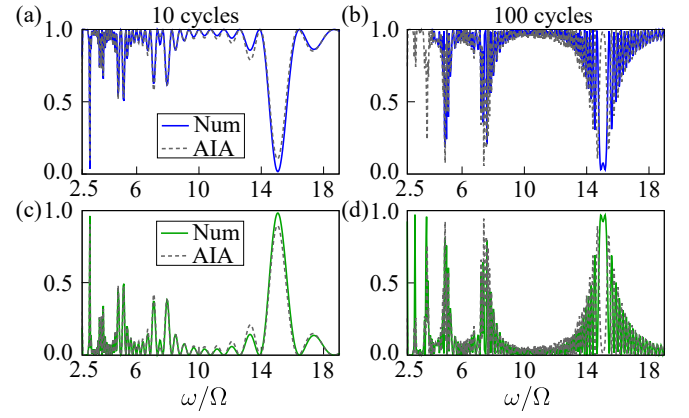


Figure 17. The numerical results (solid lines) for the populations in the adiabatic states, and the same from the AIA (dashed lines) after 10 (left column) and 100 (right column) cycles, as a function of ω for the initial state $|1\rangle \sim |gg\rangle$, $\Delta_0 = -15\Omega$, $V_0 = 40\Omega$ and $\delta = 25\Omega$. (a) and (b) show the population in $|1\rangle$, and (c) and (d) show the population in $|2\rangle$.

volved in the quenching process; one is the LZT time τ_{LZ1} across the avoided crossing. The two others: $T_a = \tau_1^{(1)} - \tau_0^{(1)} = (\pi - 2 \arcsin(-\Delta_0/\delta)) / \omega$ and $T'_a = \tau_2^{(1)} - \tau_1^{(1)} = (\pi + 2 \arcsin(-\Delta_0/\delta)) / \omega$ are the duration of adiabatic regimes between the two LZTs [see Fig. 16(a)]. We have $T'_a > T_a$ for $\Delta_0 < 0$, and the validity of AIA requires $\tau_{LZ1} \ll T_a$. Keeping δ , Δ_0 and V_0 fixed, and for sufficiently large values of ω , the ratio $\tau_{LZ1}/T_a \propto \sqrt{\omega}$ indicating that AIA breaks down at large ω .

The numerical results for the populations in the adiabatic states $\{|1\rangle, |2\rangle, |3\rangle\}$, and the same from the AIA after 10 and 100 cycles, as a function of ω , are shown in Fig. 17 for the initial state $|\psi(t=0)\rangle = |1\rangle \sim |gg\rangle$, $\Delta_0 = -15\Omega$, $V_0 = 40\Omega$ and $\delta = 25\Omega$. For these cases, the population in the state $|3\rangle$ is not very significant hence, not shown. As one can see, the interference between the LZTs at different times leads to non-trivial oscillations in the final populations as a function of ω . Higher the number of cycles, the more non-trivial the pattern is. As expected, the numerical results are well captured by AIA for lower frequencies and start to deviate at larger frequencies. Fig. 18(a) shows the time average populations in states $(|1\rangle, |2\rangle)$ as a function of ω for a period of 100 cycles with the initial state $|1\rangle$, and other parameters are the same as that of Fig. 17. The resonances at $n\omega = |\Delta_0|$ are indicated by dips (peaks) in the time-averaged population of the state $|1\rangle$ ($|2\rangle$). At the resonances, the system exhibit coherent Rabi oscillations between $|gg\rangle$ and $|s\rangle$ states [see Fig. 18(b)]. Since only two states are involved in the dynamics for this case, resonant Rabi oscillations also take place between $|1\rangle$ and $|2\rangle$ [see Fig. 18(c)], with no population in $|3\rangle$ or $|rr\rangle$ state. Thus, we have dynamics identical to that of a fully blockaded two Rydberg atoms under no periodic forcing. Following the similar procedure given in Sec. II A for the single atom case, we ob-

tain the transition probability to the state $|2\rangle$ after k -cycles is

$$P_2^k = 4(1 - P'_{LZ})P'_{LZ} \sin^2 \phi_s \frac{\sin^2 k\alpha}{\sin \alpha} \quad (25)$$

where $P'_{LZ} = \exp(-2\pi\Omega'^2/4v_1)$ with $\Omega' = \Delta E_0$, and $\cos \alpha = \text{Re}((1 - P'_{LZ})e^{-i\eta_0} + P'_{LZ}e^{-i\eta_1})$ and $\phi_s = \int_{\tau_0^{(1)}}^{\tau_1^{(1)}} (E_2 - E_1)dt/2 + \tilde{\phi}'_s$. The phases η_0 and η_1 is a function of dynamical phases acquired during the adiabatic evolution, and $\tilde{\phi}'_s$ is given by Eq. (22) but replacing v by v_1 . Note that Eq. (25) is identical to that for a single two-level atom, and hence, all the discussions followed in Secs. II A and II B are applicable here, assuming AIA is valid. Also, as $t \rightarrow \infty$, the resonances at $n\omega = 2\Delta_0 - V_0$ become relevant. The later results in a significant population in $|3\rangle$ or $|rr\rangle$ in the actual dynamics. But, the states $|3\rangle$ or $|rr\rangle$ is not involved in the LZT provided by the matrix $\hat{G}1_{LZ}$, and it implies that AIA breaks down at those resonances.

Changing the initial state to $|\psi(t=0)\rangle = |2\rangle \sim |s\rangle$ the most prominent resonances appear in the average populations are again $n\omega = |\Delta_0|$ for 10 cycles (results are not shown). Thus, obtaining similar dynamics as that for the initial state $|1\rangle$ except that the role of $|1\rangle$ and $|2\rangle$ are interchanged. For 100 cycles, in the numerical results, we have seen the emergence of resonances at $n\omega = \Delta_0 - V_0$, which are comparatively narrower than those at $n\omega = |\Delta_0|$ [see Fig. 19(a)]. The resonances at $n\omega = \Delta_0 - V_0$ indicate coherent Rabi oscillations between the states $|s\rangle$ and $|rr\rangle$ and are not captured in the AIA. For the initial state $|\psi(t=0)\rangle = |3\rangle \sim |rr\rangle$, as expected, we do not observe any signature of resonances at $n\omega = |\Delta_0|$ in the time-averaged population over 100 cycles [see Fig. 19(b)]. But, those at $n\omega = 2\Delta_0 - V_0$ and $n\omega = \Delta_0 - V_0$ are seen in the exact numerics, with the latter being much more pronounced than the former. The latter indicates that the resonances at $n\omega = 2\Delta_0 - V_0$ much narrower than those at $n\omega = \Delta_0 - V_0$. Since $|3\rangle$ is not involved in the LZT matrix $\hat{G}1_{LZ}$, the results from AIA do not show any dynamics. As a concluding remark for this section, in a multi-level periodically driven system, AIA might not capture the real dynamics due to resonances that involve states which are not directly taking place in the LZTs.

2. $\delta = 3V_0/4 - \Delta_0$

Here, we periodically drive across the first two LZTs, and the maximum of $\Delta(t)$ comes in between the second and the third avoided crossings [see Figs. 14(b) and 20]. In contrast to the previous case, here, all three states are involved in the LZTs. There are two LZT times: τ_{LZ1} and τ_{LZ2} for the transitions at $\Delta(t) = 0$ and $\Delta(t) = V_0/2$, respectively. The LZTs at $\tau_{2n}^{(1)}$ and $\tau_{2n}^{(2)}$ are characterized by the transition matrices $\hat{G}1_{LZ}$ and $\hat{G}2_{LZ}$ with v being replaced by v_1 and v_2 , respectively. There are four different adiabatic intervals [see Fig. 19], and as far as the validity of AIA is concerned, only the shortest among them matters. Once we fix $\delta = 3V_0/4 - \Delta_0$, the shortest adiabatic duration in the AIA is given by $T_a = \tau_0^{(2)} - \tau_0^{(1)} = [\sin^{-1}(-[\Delta_0 - V_0/2]/\delta) - \sin^{-1}(-\Delta_0/\delta)]/\omega$,

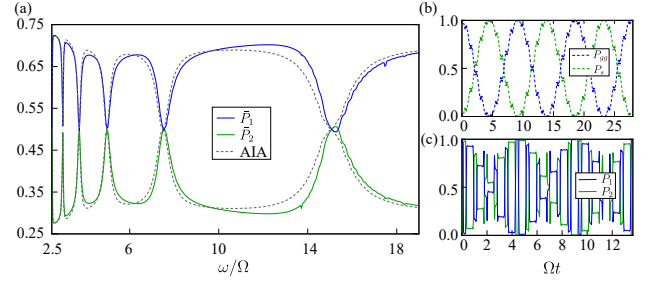


Figure 18. (a) The numerical results (solid lines) for the time-averaged populations ($\bar{P}_{1,2}$) in the adiabatic states, and the same from the AIA (dashed lines) over a period of 100 cycles, as a function of ω for the initial state $|1\rangle \sim |gg\rangle$, $\Delta_0 = -15\Omega$, $V_0 = 40\Omega$ and $\delta = 25\Omega$. The dips (peaks) in \bar{P}_1 (\bar{P}_2) indicate the resonances at $n\omega = |\Delta_0|$ at which the system exhibits coherent Rabi oscillations between $|gg\rangle$ and $|s\rangle$ or equivalently between $|1\rangle$ and $|2\rangle$ states. The six resonances are seen at $\omega/\Omega = 15, 7.5, 5, 3.75, 3, 2.5$ corresponds to $n = 1, 2, 3, 4, 5, 6$, respectively. (b) shows the coherent oscillation between $|gg\rangle$ and $|s\rangle$ at the resonance $\omega/\Omega = 7.5$ and (c) shows the same between $|1\rangle$ and $|2\rangle$ states.

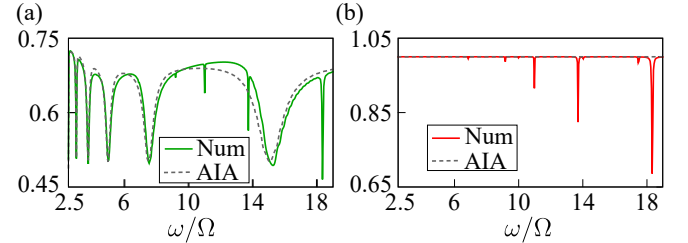


Figure 19. (a) The numerical results (solid lines) and the same from the AIA (dashed lines) for \bar{P}_2 as a function of ω for the initial state $|2\rangle \sim |s\rangle$. The dips indicate the resonances, and the five of them seen are at $\omega/\Omega = 15, 7.5, 5, 3.75, 3$ correspond to $n\omega = |\Delta_0|$ with $n = 1, 2, 3, 4, 5$, respectively. The sharp ones at $\omega/\Omega = 18.33, 13.75, 11$ correspond to $n\omega = |\Delta_0 - V_0|$ with $n = 3, 4, 5$, respectively. (b) The same for \bar{P}_3 but with the initial state $|3\rangle$. For both plots the average is taken over 100 cycles, $\Delta_0 = -15\Omega$, $V_0 = 40\Omega$ and $\delta = 25\Omega$. The three dominant dips in \bar{P}_3 are at $\omega/\Omega = 18.33, 13.75, 11$ correspond to $n\omega = |\Delta_0 - V_0|$ with $n = 3, 4, 5$, respectively.

and the validity of AIA requires $T_a \gg \tau_{LZ1}, \tau_{LZ2}$. Again, the latter implies that for large values ω , the AIA might breaks down. With two avoided crossings, the evolution matrix for one complete cycle [see Fig. 20(b)] becomes $\hat{F} = \hat{U}_5 \hat{G}1_{LZ}^T \hat{U}_4 \hat{G}2_{LZ}^T \hat{U}_3 \hat{G}2_{LZ} \hat{U}_2 \hat{G}1_{LZ} \hat{U}_1$ and for k -cycles it is \hat{F}^k .

Fig. 21 shows the time average populations in the adiabatic states as a function of ω for a period of 10 and 100 cycles for the initial state $|\psi(t=0)\rangle = |1\rangle \sim |gg\rangle$, $\Delta_0 = -15\Omega$, $V_0 = 40\Omega$ and $\delta = 45\Omega$. By comparing Fig. 21(a) and Fig. 21(b), we can see that with more number of cycles, some of the sharper resonances also got resolved. Also, the main difference from the case discussed in Sec. III B 1 is that the population \bar{P}_3 also captures resonances due to the presence of the second avoided crossing. For $k = 10$, the dips (peaks) in \bar{P}_1 (\bar{P}_2) [see Fig. 21(a)] correspond to the resonances, $n\omega = |\Delta_0|$, identical to those in Fig. 18 (for $k = 100$ and $\delta/\Omega = 25$). Here, with

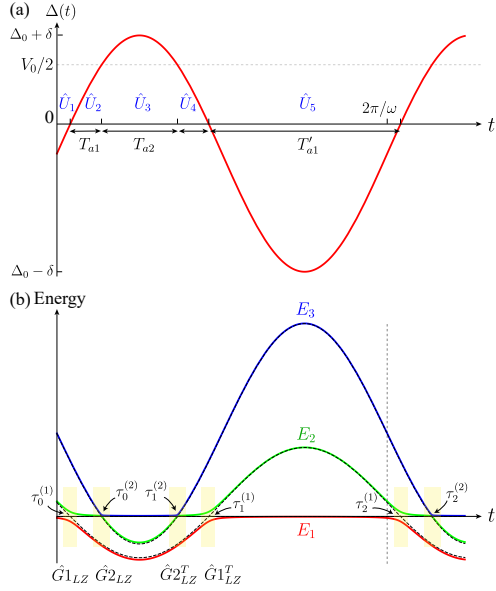


Figure 20. (a) The periodic time dependence of the detuning for $\delta = 3V_0/4 - \Delta_0$. The durations in which adiabatic evolution takes place in AIA is marked by T_{a1} , T_{a2} , and T'_{a1} . (b) shows the corresponding instantaneous energy eigenvalues. The instants $(\tau_0^{(1)}, \tau_0^{(2)}, \tau_1^{(1)}, \tau_1^{(2)}, \tau_2^{(1)}, \tau_2^{(2)})$ at which the LZTs occur between different adiabatic states are shown by shaded stripes. Between each of these LZTs, adiabatic evolution takes place. The \hat{U} and \hat{G} operators represent the adiabatic regime and non-adiabatic transition points, respectively. Between the origin and the dashed vertical line, we have one complete cycle.

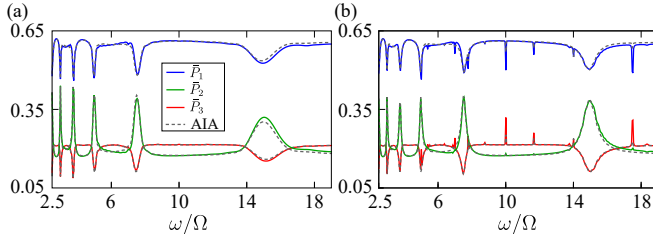


Figure 21. The numerical results (solid lines) for the time-averaged populations $(\bar{P}_{1,2,3})$ in the adiabatic states, and the same from the AIA (dashed lines) for a period of (a) 10 and (b) 100 cycles, as a function of ω for the initial state $|1\rangle \sim |gg\rangle$, $\Delta_0 = -15\Omega$, $V_0 = 40\Omega$ and $\delta = 45\Omega$. The dips (peaks) in \bar{P}_1 (\bar{P}_2) indicates the resonances $n\omega = |\Delta_0|$ and are the same as that in Fig. 19(a). The sharper resonances in (b) correspond to antiblockades occurring at $n\omega = 2\Delta_0 - V_0$, and the two pronounced ones are seen at $\omega/\Omega = 17.5, 10$.

$\delta/\Omega = 45$ and making $k = 100$, we can resolve the narrow resonances at $n\omega = 2\Delta_0 - V_0$ (between $|gg\rangle$ and $|rr\rangle$ states) and the two pronounced ones are seen at $\omega/\Omega = 17.5, 10$ [see Fig. 21(b)]. AIA does not capture the latter resonances since the third avoided crossing in which the resonant transition between $|s\rangle$ and $|rr\rangle$ are missing. Therefore AIA misses any resonances in which $|rr\rangle$ is populated from $|gg\rangle$ via $|s\rangle$.

Figs. 22(a) and 22(b) show the time average populations in the adiabatic states as a function of ω for a period of 100 cycles for the initial state $|\psi(t=0)\rangle = |2\rangle \sim |s\rangle$ and

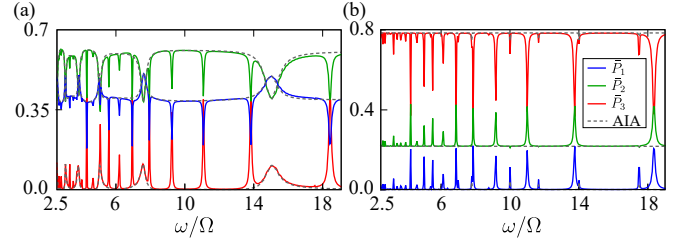


Figure 22. The numerical results (solid lines) for the time-averaged populations $(\bar{P}_{1,2,3})$ in the adiabatic states, and the same from the AIA (dashed lines) for a period of 100 cycles, as a function of ω for the initial state (a) $|2\rangle \sim |s\rangle$ and (b) $|3\rangle \sim |rr\rangle$. Other parameters are $\Delta_0 = -15\Omega$, $V_0 = 40\Omega$ and $\delta = 45\Omega$. In (a) we see resonances correspond to $n\omega = |\Delta_0|$ (between $|gg\rangle$ and $|s\rangle$ states) and $n\omega = |\Delta_0 - V_0|$ (between $|rr\rangle$ and $|s\rangle$ states) whereas in (b) the resonances appear are those correspond to the transitions between $|rr\rangle$ and $|s\rangle$, and $|rr\rangle$ and $|gg\rangle$.

$|\psi(t=0)\rangle = |3\rangle \sim |rr\rangle$, respectively. The other parameters are the same as that of Fig. 21. In contrast with the case of initial state $|1\rangle$ [see Fig. 21(b)], more resonances are resolved by taking the initial state as either $|s\rangle$ [see Fig. 22(a)] or $|rr\rangle$ [see Fig. 22(b)]. For the initial state $|s\rangle$, the resonances correspond to the transition between $|s\rangle$ and $|gg\rangle$ ($n\omega = |\Delta_0|$), and $|s\rangle$ and $|rr\rangle$ ($n\omega = |\Delta_0 - V_0|$) signify in the average populations of all three states. On the other hand, with the initial state $|rr\rangle$, the average populations did not capture the resonances at $n\omega = |\Delta_0|$, whereas those corresponding to the transitions between $|rr\rangle$ and $|s\rangle$, and $|rr\rangle$ and $|gg\rangle$ appear. Also, AIA completely failed with the initial state $|3\rangle \sim |rr\rangle$, since no LZTs are involved.

3. $\delta = 5V_0/4 - \Delta_0$

For the last case, the modulation amplitude is such that the system drives past all three avoided crossings. There are three LZT times involved in the dynamics: τ_{LZ1} , τ_{LZ2} , and τ_{LZ3} for the transitions at $\Delta(t) = 0$, $\Delta(t) = V_0/2$ and $\Delta(t) = V_0$, respectively. Note that, $\tau_{LZ2} \ll \tau_{LZ1}, \tau_{LZ3}$. As far as the validity of AIA is concerned, the shortest duration of adiabatic evolution [T_{a1} in Fig. 23(a)] should be larger than both τ_{LZ1} and τ_{LZ3} . Including all three avoided crossings, in the AIA, the evolution matrix for one complete cycle [see Fig. 23] becomes $\hat{F} = \hat{U}_7 \hat{G}^T_{1LZ} \hat{U}_6 \hat{G}^T_{2LZ} \hat{U}_5 \hat{G}^T_{3LZ} \hat{U}_4 \hat{G}^T_{3LZ} \hat{U}_3 \hat{G}^T_{2LZ} \hat{U}_2 \hat{G}^T_{1LZ} \hat{U}_1$ and for k -cycles it is \hat{F}^k . The LZT matrices \hat{G}^T_{1LZ} and \hat{G}^T_{2LZ} are provided by Eqs. (21) and (23), with v being replaced by v_1 and v_2 , respectively. The third LZT matrix is,

$$\hat{G}^T_{3LZ} = \begin{pmatrix} 1 & 0 & 0 \\ 0 & \sqrt{1 - P''''_{LZ}} e^{-i\tilde{\phi}_{s3}} & -\sqrt{P''''_{LZ}} \\ 0 & \sqrt{P''''_{LZ}} & \sqrt{1 - P''''_{LZ}} e^{i\tilde{\phi}_{s3}} \end{pmatrix}$$

where $P''''_{LZ} = \exp(-2\pi\Omega''''^2/4v_3)$ with $\Omega''' = \Delta E_{V_0}$, $\tilde{\phi}_{s3} = \frac{\pi}{4} + \arg(\Gamma(1 - iy''')) + \gamma'''(\ln \gamma''' - 1)$ with $\gamma''' = \Omega''''^2/4v_3$ and $v_3 = \omega\sqrt{\delta^2 - (\Delta_0 - V_0)^2}$, and the \hat{U} s are the adiabatic evolution matrices.

In Fig. 24 we show the time average populations in the adiabatic states as a function of ω for a period of 100 cycles, $\Delta_0 =$

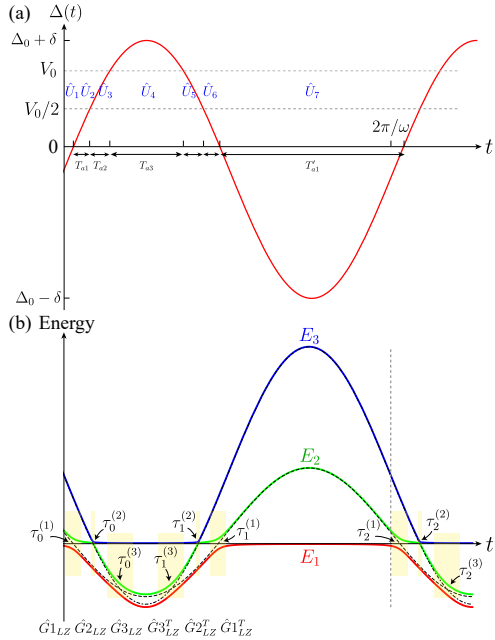


Figure 23. (a) The periodic time dependence of the detuning for $\delta = 5V_0/4 - \Delta_0$. The durations in which adiabatic evolution takes place in AIA is marked by T_{a1} , T_{a2} , T_{a3} , and T'_{a1} . (b) shows the corresponding instantaneous energy eigenvalues. The instants $(\tau_0^{(1)}, \tau_0^{(2)}, \tau_0^{(3)}, \tau_1^{(3)}, \tau_1^{(2)}, \tau_1^{(1)}, \tau_2^{(1)}, \tau_2^{(2)}, \tau_2^{(3)})$ at which the LZTs occur between different adiabatic states are shown by shaded stripes. Between each of these LZTs, adiabatic evolution takes place. The \hat{U} and \hat{G} operators represent the adiabatic regime and non-adiabatic transition points, respectively. Between the origin and the dashed vertical line, we have one complete cycle.

-15Ω , $V_0 = 40\Omega$, $\delta = 65\Omega$, and for all three initial states. In Fig. 24(a), for the initial state $|\psi(t=0)\rangle = |1\rangle \sim |gg\rangle$, we observe major peaks corresponding to the resonances $n\omega = |\Delta_0|$ (between $|gg\rangle$ and $|s\rangle$ states), and minor ones indicate the resonances at $n\omega = |2\Delta_0 - V_0|$ (between $|gg\rangle$ and $|rr\rangle$ states). For the initial state $|\psi(t=0)\rangle = |2\rangle \sim |s\rangle$ [see Fig. 24(b)] we observe resonances at $n\omega = |\Delta_0|$ and $n\omega = |\Delta_0 - V_0|$, with no traces on the resonances at $n\omega = |2\Delta_0 - V_0|$. Finally, for the initial state $|\psi(t=0)\rangle = |3\rangle \sim |rr\rangle$, except the resonances at $n\omega = |\Delta_0|$, other two are captured. Note that, by including all three avoided crossings, the results from AIA are in excellent agreement with exact numerical results, and in particular, all

resonance features have been captured.

C. Summary

In summary, we analyzed the LZ dynamics comprehensively in a setup of two Rydberg-atoms with a time-dependent detuning, both linear and periodic, using both the exact numerical calculations as well as the method of AIA. The Rydberg-atom setup realizes different three-level LZ models, for instance, for vanishingly small Rydberg interactions, it converges to a bow-tie model. For sufficiently large interactions, we have a triangular LZ model. The latter is known to exhibit beats and step patterns in the population dynamics. In general, the LZ dynamics show a non-trivial dependence on the initial state, the quench rate of the detuning across avoided crossings, and the interaction strength. Under suitable criteria, the dynamics are well captured by the AIA especially, at large interactions for which the distinct LZ transitions can be isolated from each other by adiabatic regimes. Finally, we analyzed the dynamics in the two-atom setup with periodically modulated detuning, with sufficiently large Rydberg interactions such that all level crossings are well separated. Based on the driving amplitude, the initial states, and the number of avoided crossings are driven across, different scenarios are discussed. When the detuning is modulated across the first avoided crossing, at shorter periods, the dynamics are found identical to that of a two-level atom. At more extended periods, due to resonances, all the three levels become relevant, which also results in the violation of AIA. When the detuning is modulated across either two or all three level crossings, more and more resonances emerge in the population dynamics. The latter also found to be depending on the initial state. For the last case, involving all three avoided crossings, the AIA entirely captures the resulting resonances, whereas in other cases it only did partially.

D. Acknowledgments

We acknowledge UKIERI- UGC Thematic Partnership No. IND/CONT/G/16-17/73 UKIERI-UGC project, UGC for UGC-CSIR NET-JRF/SRF, the support from the EP-SRC through Grant No. EP/M014266/1 and Grant No. EP/R04340X/1 via the QuantERA project ERyQSenS.

[1] L. D. Landau, *Phys. Z. Sowjetunion* **2**, 46 (1932).
[2] C. Zener, *Proc. R. Soc. Lond. A* **137**, 696 (1932).
[3] C. E. Carroll and F. T. Hioe, *J. Phys. A: Math. Gen.*, **19**, 2061 (1986).
[4] Y. N. Demkov and V. N. Ostrovsky, *Phys. Rev. A* **61**, 032705 (2000).
[5] M. Førre and J. P. Hansen, *Phys. Rev. A* **67**, 053402 (2003).
[6] A. V. Shytov, *Phys. Rev. A* **70**, 052708 (2004).
[7] Y. B. Band and Y. Avishai, *Phys. Rev. A* **99**, 032112 (2019).
[8] M. B. Kenmoe and L. C. Fai, *Phys. Rev. B* **94**, 125101 (2016).
[9] M. N. Kiselev, K. Kikoin, and M. B. Kenmoe, *Eur. Phys. Lett.* **104**, 57004 (2013).
[10] S. Ashhab, *Phys. Rev. A* **94**, 042109 (2016).
[11] N. A. Sinitsyn, *J. Phys. A: Math. The.* **48**, 195305 (2015).
[12] N. A. Sinitsyn and F. Li, *Phys. Rev. A* **93**, 063859 (2016).
[13] N. A. Sinitsyn and V. Y. Chernyak, *J. Phys. A*, **50**, 255203 (2017).
[14] F. Li, C. Sun, V. Y. Chernyak, and N. A. Sinitsyn, *Phys. Rev. A* **96**, 022107 (2017).

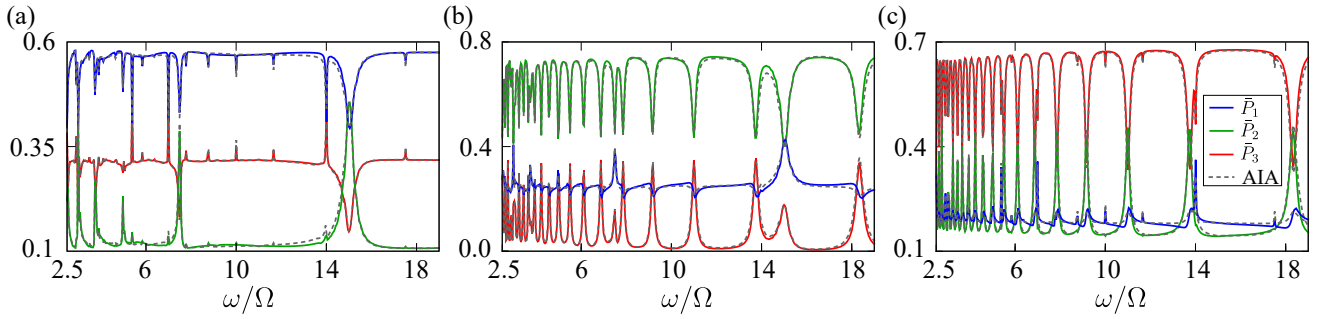


Figure 24. The numerical results (solid lines) for the time-averaged populations ($\bar{P}_{1,2,3}$) in the adiabatic states, and the same from the AIA (dashed lines) over a period of 100 cycles, as a function of ω for the initial state (a) $|1\rangle$, (b) $|2\rangle$ and (c) $|3\rangle$. Other parameters are $\Delta_0 = -15\Omega$, $V_0 = 40\Omega$ and $\delta = 65\Omega$. In (a) the major peaks correspond to the resonances $n\omega = |\Delta_0|$ (between $|gg\rangle$ and $|s\rangle$ states) and smaller ones indicate the resonances at $n\omega = |\Delta_0 - V_0|$ (between $|rr\rangle$ and $|s\rangle$ states). In (b) the peaks/dips indicate the resonances at $n\omega = |\Delta_0|$ and $n\omega = |\Delta_0 - V_0|$, with no traces on the resonances at $n\omega = |2\Delta_0 - V_0|$. In (c) except the resonances at $n\omega = |\Delta_0|$, other two types are seen. AIA results are in excellent agreement with numerics in all three cases.

- [15] N. A. Sinitsyn, J. Lin, and V. Y. Chernyak, *Phys. Rev. A* **95**, 012140 (2017).
- [16] A. V. Parafilo and M. N. Kiselev, *L. Temp. Phys.* **44**, 1325 (2018).
- [17] B. Militello, *Phys. Rev. A* **99**, 063412 (2019).
- [18] Y.-A. Chen, S. D. Huber, S. Trotzky, I. Bloch, and E. Altman, *Nat. Phys.* **7**, 61 EP (2010).
- [19] Q. Niu, X.-G. Zhao, G. A. Georgakis, and M. G. Raizen, *Phys. Rev. Lett.* **76**, 4504 (1996).
- [20] B. Wu and Q. Niu, *Phys. Rev. A* **61**, 023402 (2000).
- [21] J.-Y. Yan, S. Duan, W. Zhang, and X.-G. Zhao, *Phys. Rev. A* **79**, 053613 (2009).
- [22] T. Salger, C. Geckeler, S. Kling, and M. Weitz, *Phys. Rev. Lett.* **99**, 190405 (2007).
- [23] C. Kasztelan, S. Trotzky, Y.-A. Chen, I. Bloch, I. P. McCulloch, U. Schollwöck, and G. Orso, *Phys. Rev. Lett.* **106**, 155302 (2011).
- [24] S. F. Caballero-Benítez and R. Paredes, *Phys. Rev. A* **85**, 023605 (2012).
- [25] J. Larson, *Eur. Phys. Lett.* **107**, 30007 (2014).
- [26] H. Zhong, Q. Xie, J. Huang, X. Qin, H. Deng, J. Xu, and C. Lee, *Phys. Rev. A* **90**, 023635 (2014).
- [27] S. N. Shevchenko, S. Ashhab, and F. Nori, *Phys. Rep.* **492**, 1 (2010).
- [28] C. S. E. van Ditzhuijzen, A. Tauschinsky, and H. B. van Linden van den Heuvell, *Phys. Rev. A* **80**, 063407 (2009).
- [29] A. V. Shytov, D. A. Ivanov, and M. V. Feigel'man, *Eur. Phys. J. B* **36**, 263 (2003).
- [30] M. Sillanpää, T. Lehtinen, A. Paila, Y. Makhlin, and P. Hakonen, *Phys. Rev. Lett.* **96**, 187002 (2006).
- [31] W. D. Oliver, Y. Yu, J. C. Lee, K. K. Berggren, L. S. Levitov, and T. P. Orlando, *Science* **310**, 1653 (2005).
- [32] C. M. Wilson, T. Duty, F. Persson, M. Sandberg, G. Johansson, and P. Delsing, *Phys. Rev. Lett.* **98**, 257003 (2007).
- [33] A. Izmalkov, S. H. W. van der Ploeg, S. N. Shevchenko, M. Grajcar, E. Il'ichev, U. Hübner, A. N. Omelyanchouk, and H.-G. Meyer, *Phys. Rev. Lett.* **101**, 017003 (2008).
- [34] J. Stehlik, Y. Dovzhenko, J. R. Petta, J. R. Johansson, F. Nori, H. Lu, and A. C. Gossard, *Phys. Rev. B* **86**, 121303 (2012).
- [35] E. Dupont-Ferrier, B. Roche, B. Voisin, X. Jehl, R. Wacquez, M. Vinet, M. Sanquer, and S. De Franceschi, *Phys. Rev. Lett.* **110**, 136802 (2013).
- [36] G. Cao, H.-O. Li, T. Tu, L. Wang, C. Zhou, M. Xiao, G.-C. Guo, H.-W. Jiang, and G.-P. Guo, *Nat. Commun.* **4**, 1401 EP (2013).
- [37] F. Forster, G. Petersen, S. Manus, P. Hänggi, D. Schuh, W. Wegscheider, S. Kohler, and S. Ludwig, *Phys. Rev. Lett.* **112**, 116803 (2014).
- [38] T. Ota, K. Hitachi, and K. Muraki, *Sci. Rep.* **8**, 5491 (2018).
- [39] H. Liu, M. Dai, and L. F. Wei, *Phys. Rev. A* **99**, 013820 (2019).
- [40] F. Grossmann, T. Dittrich, P. Jung, and P. Hänggi, *Phys. Rev. Lett.* **67**, 516 (1991).
- [41] S. Raghavan, V. M. Kenkre, D. H. Dunlap, A. R. Bishop, and M. I. Salkola, *Phys. Rev. A* **54**, R1781 (1996).
- [42] G. S. Agarwal and W. Harshwardhan, *Phys. Rev. A* **50**, R4465 (1994).
- [43] M. W. Noel, W. M. Griffith, and T. F. Gallagher, *Phys. Rev. A* **58**, 2265 (1998).
- [44] K. Saito and Y. Kayanuma, *Phys. Rev. B* **70**, 201304 (2004).
- [45] L. Gaudreau, G. Granger, A. Kam, G. C. Aers, S. A. Stukenikin, P. Zawadzki, M. Pioro-Ladrière, Z. R. Wasilewski, and A. S. Sachrajda, *Nat. Phys.* **8**, 54 EP (2011).
- [46] M. P. Silveri, J. A. Tuorila, E. V. Thuneberg, and G. S. Paraoanu, *Rep. Prog. Phys.* **80**, 056002 (2017).
- [47] D. A. Abanin, W. De Roeck, and F. Huveneers, *Ann. Phys.* **372**, 1 (2016).
- [48] P. Ponte, A. Chandran, Z. Papić, and D. A. Abanin, *Ann. Phys.* **353**, 196 (2015).
- [49] B. Damski, *Phys. Rev. Lett.* **95**, 035701 (2005).
- [50] J. Dziarmaga, M. Tylutki, and W. H. Zurek, *Phys. Rev. B* **86**, 144521 (2012).
- [51] B. Damski and W. H. Zurek, *Phys. Rev. A* **73**, 063405 (2006).
- [52] J. Dziarmaga, *Adv. Phys.* **59**, 1063 (2010).
- [53] L. D'Alessio and A. Polkovnikov, *Ann. Phys.* **333**, 19 (2013).
- [54] M. Bukov, L. D'Alessio, and A. Polkovnikov, *Ad. Phy.* **64**, 139 (2015).
- [55] A. Eckardt, *Rev. Mod. Phys.* **89**, 011004 (2017).
- [56] M. Saffman, T. G. Walker, and K. Mølmer, *Rev. Mod. Phys.* **82**, 2313 (2010).
- [57] M. D. Lukin, M. Fleischhauer, R. Cote, L. M. Duan, D. Jaksch, J. I. Cirac, and P. Zoller, *Phys. Rev. Lett.* **87**, 037901 (2001).
- [58] E. Urban, T. A. Johnson, T. Henage, L. Isenhower, D. D. Yavuz, T. G. Walker, and M. Saffman, *Nat. Phys.* **5**, 110 (2009).

[59] A. Gaëtan, Y. Miroshnychenko, T. Wilk, A. Chotia, M. Viteau, D. Comparat, P. Pillet, A. Browaeys, and P. Grangier, *Nat. Phys.* **5**, 115 (2009).

[60] R. Heidemann, U. Raitzsch, V. Bendkowsky, B. Butscher, R. Löw, L. Santos, and T. Pfau, *Phys. Rev. Lett.* **99**, 163601 (2007).

[61] C. Ates, T. Pohl, T. Pattard, and J. M. Rost, *Phys. Rev. Lett.* **98**, 023002 (2007).

[62] J. Qian, Y. Qian, M. Ke, X.-L. Feng, C. H. Oh, and Y. Wang, *Phys. Rev. A* **80**, 053413 (2009).

[63] T. Amthor, C. Giese, C. S. Hofmann, and M. Weidemüller, *Phys. Rev. Lett.* **104**, 013001 (2010).

[64] S. Basak, Y. Chougale, and R. Nath, *Phys. Rev. Lett.* **120**, 123204 (2018).

[65] X.-R. Huang, Z.-X. Ding, C.-S. Hu, L.-T. Shen, W. Li, H. Wu, and S.-B. Zheng, *Phys. Rev. A* **98**, 052324 (2018).

[66] J.-L. Wu, J. Song, and S.-L. Su, *Phys. Lett. A*, 126039 (2019).

[67] S. H. Autler and C. H. Townes, *Phys. Rev.* **100**, 703 (1955).

[68] T. F. Gallagher and P. Pillet, “Dipole–dipole interactions of rydberg atoms,” in *Advances In Atomic, Molecular, and Optical Physics*, Vol. 56 (Academic Press, 2008) pp. 161–218.

[69] V. Zhelyazkova and S. D. Hogan, *Mol. Phys.* **113**, 3979 (2015).

[70] D. B. Tretyakov, V. M. Entin, E. A. Yakshina, I. I. Beterov, C. Andreeva, and I. I. Ryabtsev, *Phys. Rev. A* **90**, 041403 (2014).

[71] V. Zhelyazkova and S. D. Hogan, *Phys. Rev. A* **92**, 011402 (2015).

[72] A. Tauschinsky, C. S. E. van Ditzhuijzen, L. D. Noordam, and H. B. v. L. van den Heuvell, *Phys. Rev. A* **78**, 063409 (2008).

[73] P. Bohloli-Zanjani, J. A. Petrus, and J. D. D. Martin, *Phys. Rev. Lett.* **98**, 203005 (2007).

[74] N. Saquet, A. Cournol, J. Beugnon, J. Robert, P. Pillet, and N. Vanhaecke, *Phys. Rev. Lett.* **104**, 133003 (2010).

[75] J. R. Rubbmark, M. M. Kash, M. G. Littman, and D. Kleppner, *Phys. Rev. A* **23**, 3107 (1981).

[76] F. Robicheaux, C. Wesdorp, and L. D. Noordam, *Phys. Rev. A* **62**, 043404 (2000).

[77] C. W. S. Conover, M. C. Doogue, and F. J. Struwe, *Phys. Rev. A* **65**, 033414 (2002).

[78] J. Lambert, M. W. Noel, and T. F. Gallagher, *Phys. Rev. A* **66**, 053413 (2002).

[79] A. Gütler and W. J. van der Zande, *Phys. Lett. A* **324**, 315 (2004).

[80] H. Maeda, J. H. Gurian, and T. F. Gallagher, *Phys. Rev. A* **83**, 033416 (2011).

[81] R. Feynman, J. Hollingsworth, M. Vennettilli, T. Budner, R. Zmiewski, D. P. Fahey, T. J. Carroll, and M. W. Noel, *Phys. Rev. A* **92**, 043412 (2015).

[82] S. S. Zhang, W. Gao, H. Cheng, L. You, and H. P. Liu, *Phys. Rev. Lett.* **120**, 063203 (2018).

[83] S. Ashhab, J. R. Johansson, A. M. Zagoskin, and F. Nori, *Phys. Rev. A* **75**, 063414 (2007).

[84] B. M. Garraway and N. V. Vitanov, *Phys. Rev. A* **55**, 4418 (1997).

[85] N. V. Vitanov, *Phys. Rev. A* **59**, 988 (1999).

[86] S. N. Shevchenko, S. Ashhab, and F. Nori, *Phys. Rev. B* **85**, 094502 (2012).

[87] C. Roychoudhuri, *Am. J. Phys.* **43**, 1054 (1975).

[88] L. Béguin, A. Vernier, R. Chicireanu, T. Lahaye, and A. Browaeys, *Phys. Rev. Lett.* **110**, 263201 (2013).

[89] T. Wilk, A. Gaëtan, C. Evellin, J. Wolters, Y. Miroshnychenko, P. Grangier, and A. Browaeys, *Phys. Rev. Lett.* **104**, 010502 (2010).

[90] L. Isenhower, E. Urban, X. L. Zhang, A. T. Gill, T. Henage, T. A. Johnson, T. G. Walker, and M. Saffman, *Phys. Rev. Lett.* **104**, 010503 (2010).

[91] I. I. Ryabtsev, D. B. Tretyakov, I. I. Beterov, and V. M. Entin, *Phys. Rev. Lett.* **104**, 073003 (2010).

[92] S. Ravets, H. Labuhn, D. Barredo, L. Béguin, T. Lahaye, and A. Browaeys, *Nat. Phys.* **10**, 914 EP (2014).

[93] H. Labuhn, S. Ravets, D. Barredo, L. Béguin, F. Nogrette, T. Lahaye, and A. Browaeys, *Phys. Rev. A* **90**, 023415 (2014).

[94] S. Ravets, H. Labuhn, D. Barredo, T. Lahaye, and A. Browaeys, *Phys. Rev. A* **92**, 020701 (2015).

[95] Y. Y. Jau, A. M. Hankin, T. Keating, I. H. Deutsch, and G. W. Biedermann, *Nat. Phys.* **12**, 71 EP (2015).

[96] S. de Léséleuc, D. Barredo, V. Lienhard, A. Browaeys, and T. Lahaye, *Phys. Rev. Lett.* **119**, 053202 (2017).

[97] Y. Zeng, P. Xu, X. He, Y. Liu, M. Liu, J. Wang, D. J. Papoular, G. V. Shlyapnikov, and M. Zhan, *Phys. Rev. Lett.* **119**, 160502 (2017).

[98] C. J. Picken, R. Legaie, K. McDonnell, and J. D. Pritchard, *Quantum Science and Technology* **4**, 015011 (2018).

[99] H. Levine, A. Keesling, A. Omran, H. Bernien, S. Schwartz, A. S. Zibrov, M. Endres, M. Greiner, V. Vuletić, and M. D. Lukin, *Phys. Rev. Lett.* **121**, 123603 (2018).

[100] A. Reinhard, T. C. Liebsch, B. Knuffman, and G. Raithel, *Phys. Rev. A* **75**, 032712 (2007).

[101] V. N. Ostrovsky and H. Nakamura, *J. Phys. A: Math. Gen.* **30**, 6939 (1997).

[102] Y. N. Demkov and V. N. Ostrovsky, *J. Phys. B: At. Mol. Opt. Phys.* **34**, 2419 (2001).

[103] V. Srivastava, A. Nirajan, and R. Nath, *J. Phys. B: At. Mol. Opt. Phys.* **52**, 184001 (2019).

[104] T. Pohl, E. Demler, and M. D. Lukin, *Phys. Rev. Lett.* **104**, 043002 (2010).

[105] R. M. W. van Bijnen, S. Smit, K. A. H. van Leeuwen, E. J. D. Vredenbregt, and S. J. J. M. F. Kokkelmans, *J. Phys. B: At. Mol. Opt. Phys.* **44**, 184008 (2011).

[106] P. Schauß, J. Zeiher, T. Fukuhara, S. Hild, M. Cheneau, T. Macrì, T. Pohl, I. Bloch, and C. Gross, *Science* **347**, 1455 (2015).